

## Isogeometric simulation of acoustic radiation

Hernández Mederos, Victoria; Moreno Hernández, Eduardo; Estrada Sarlabous, Jorge; Abelló Ugalde, Isidro A.; Lahaye, Domenico

**DOI**

[10.1016/j.matcom.2023.09.018](https://doi.org/10.1016/j.matcom.2023.09.018)

**Publication date**

2024

**Document Version**

Final published version

**Published in**

Mathematics and Computers in Simulation

**Citation (APA)**

Hernández Mederos, V., Moreno Hernández, E., Estrada Sarlabous, J., Abelló Ugalde, I. A., & Lahaye, D. (2024). Isogeometric simulation of acoustic radiation. *Mathematics and Computers in Simulation*, 225, 914-938. <https://doi.org/10.1016/j.matcom.2023.09.018>

**Important note**

To cite this publication, please use the final published version (if applicable).  
Please check the document version above.

**Copyright**

Other than for strictly personal use, it is not permitted to download, forward or distribute the text or part of it, without the consent of the author(s) and/or copyright holder(s), unless the work is under an open content license such as Creative Commons.

**Takedown policy**

Please contact us and provide details if you believe this document breaches copyrights.  
We will remove access to the work immediately and investigate your claim.

***Green Open Access added to TU Delft Institutional Repository***

***'You share, we take care!' - Taverne project***

**<https://www.openaccess.nl/en/you-share-we-take-care>**

Otherwise as indicated in the copyright section: the publisher is the copyright holder of this work and the author uses the Dutch legislation to make this work public.



## Original articles

## Isogeometric simulation of acoustic radiation

Victoria Hernández Mederos<sup>a,\*</sup>, Eduardo Moreno Hernández<sup>a</sup>, Jorge Estrada Sarlabous<sup>a</sup>,  
Isidro A. Abelló Ugalde<sup>b</sup>, Domenico Lahaye<sup>c</sup><sup>a</sup> Instituto de Cibernética, Matemática y Física, ICIMAF, La Habana, Cuba<sup>b</sup> CEPES, Universidad de La Habana, Cuba<sup>c</sup> DIAM, TU Delft, The Netherlands

Received 6 January 2023; received in revised form 15 September 2023; accepted 23 September 2023

Available online 29 September 2023

**Abstract**

In this paper we discuss the numerical solution of the Helmholtz equation with mixed boundary conditions on a 2D physical domain  $\Omega$ . The so called *radiation problem* depends on the constant wavenumber  $k$ , that in some medical applications can be of order of thousands. For these values of  $k$  the classical Finite Element Method (FEM) faces up several numerical difficulties. To mitigate these limitations we apply the Isogeometric Analysis (IgA) to compute the approximated solution  $u^h$ . Main steps of IgA are discussed and specific proposals for their fulfillment are addressed, with focus on some aspects not covered in available publications. In particular, we introduce a low distortion quadratic NURBS parametrization of  $\Omega$  that represents exactly its boundary and contributes to the accuracy of  $u^h$ . Our approach is non-isoparametric since  $u^h$  is a bicubic tensor product polynomial B-spline function on  $\Omega$ . This allows to improve the numerical solution refining the approximation space and keeping the coarser parametrization of the domain. Moreover, we discuss the role of the number of degrees of freedom in the directions perpendicular and longitudinal to wave front and its relationship with the noise and the shift in amplitude and phase of  $u^h$ . The linear system derived from IgA discretization of the radiation problem is solved using GMRES and we show through experiments that the incomplete factorization of the Complex Shifted Laplacian provides a very good preconditioner. To solve the radiation problem, we have implemented IgA approach using the open source package GeoPDEs. A comparison with FEM is included, to provide evidence that IgA approach is superior since it is able to reduce significantly the pollution error, especially for high values of  $k$ , producing additionally smoother solutions which depend on less degrees of freedom. © 2023 International Association for Mathematics and Computers in Simulation (IMACS). Published by Elsevier B.V. All rights reserved.

**Keywords:** Isogeometric analysis; Helmholtz equation; Radiation problem

**1. Introduction**

Wave problems have been intensively studied since they are relevant in multiple fields. The solution of wave equation is usually written as the product of a function of time and a function  $u(x, y)$  which only depends on spacial variables. In acoustic problems, for instance, the time function is chosen as  $e^{i\omega t}$ , where  $\omega$  is the angular frequency of the propagating wave and  $i$  is the imaginary unit. With this time harmonic dependence, the wave

\* Corresponding author.

E-mail address: [vicky@icimaf.cu](mailto:vicky@icimaf.cu) (V. Hernández).

equation is reduced to the Helmholtz equation

$$-\Delta u(x, y) - k^2 u(x, y) = 0$$

where  $k = 2\pi/\lambda$  is the number of waves per unit of distance, called *wavenumber*, and  $\lambda$  is the wavelength.

Helmholtz equation is very important in acoustic applications, including seismic wave propagation, acoustic noise control, non destructive testing and medical ultrasound. In particular, therapeutic applications of ultrasound involve focused beams directing the ultrasound energy into the tissue region that needs the treatment. Currently, High Intensity Focused Ultrasound (HIFU) therapy method is known as one of the most advanced surgical [36] and also physio-therapeutical techniques [32]. In most clinical applications, HIFU transducers are excited at a single frequency in the range 0.5–8 MHz. From the mathematical point of view, Pennes' bioheat equation [47] is used to model thermal diffusion effects of HIFU. This equation relates the temperature distribution in time and space with the absorbed ultrasound energy, which is computed from the acoustic pressure field  $u(x, y)$  solution of the Helmholtz equation.

The numerical solution of Helmholtz equation is in general a challenge. When the wavenumber  $k$  is small, it can be handled using low degree Finite Element Method (FEM). But the design of robust and efficient numerical algorithms for high values of  $k$  is difficult. In practice, many numerical difficulties appear. For high values of  $k$  the function  $u(x, y)$  is very oscillatory, thus to obtain an accurate approximation of  $u(x, y)$  with finite elements it is necessary to use a large number  $N$  of degrees of freedom. Moreover, it is known [5,6,35], that even if we require that  $kh$  is a small constant, with  $h$  denoting the mesh size, (and in consequence  $N$  is large) the errors of continuous Galerkin finite element approximations increases when  $k$  becomes larger. In the literature, this non-robust behavior with respect to  $k$ , is known as the pollution effect. According to [23] pollution can be understood as the gap between the error of Galerkin solution and the best approximation that is possible with the underlying Galerkin basis. In [42] it is shown that FEM solution of degree  $p$  is quasi-optimal, if  $h^p k^{(p+1)}$  is a sufficiently small constant. It means that even when the pollution still affects high order methods, it can be reduced by increasing  $p$ . But for high values of  $k$  the condition  $h^p k^{(p+1)}$  small leads to prohibitively large linear systems with high computational cost. Moreover, for engineering applications the most important issue is that the solution attains a prescribed accuracy even if it is not the best approximation. In this sense, it is common to apply the rule of thumb  $h \approx \lambda/\tau$ , where  $\tau \geq 10$  denotes the number of degrees of freedom per wavelength.

The standard variational formulation of the Helmholtz equation is sign-indefinite (i.e. not coercive). Hence, another difficulty for the numerical solution of the Helmholtz equation is that for  $k$  sufficiently large, the coefficient matrix is indefinite and non-normal. As a consequence, iterative methods to solve the corresponding linear systems behave extremely bad if the system is not preconditioned [24,28]. To face this problem researches have proposed several preconditioners, such as multigrid methods with Krylov smoothers, domain decomposition, and complex shifted Laplacian preconditioner. The last one was introduced in [27] and further developed and successfully generalized in [31,54,55].

Dealing with wave problems, the small discrepancies between the boundary of the mesh constructed by FEM and the boundary of the physical domain  $\Omega$ , can significantly increase the error of the FEM approximated solution [20,43]. This is more evident in 3D industrial applications, where the surface of the physical domain is usually represented in terms of Nonuniform Rational B-spline functions (NURBS) [48]. Since B-spline spaces include as a particular case the piecewise polynomial spaces commonly used in FEM, it was natural to think of the possibility of writing the approximated solution of the partial differential equation (PDE) in terms of the B-spline basis functions. This idea led to the emergence of the Isogeometric Analysis (IgA), introduced by Hughes et al. in 2005 [34], as a modern method to solve PDE. IgA uses B-spline functions to parametrize the geometry  $\Omega$  and as shape functions to approximate the solution of the PDE. In this sense, it combines the variational techniques of FEM, with the classical functions in computer design systems. IgA and FEM are based on the same principle, the Galerkin method, but IgA approach has a very important advantage: B-spline basis functions may be constructed to have high smoothness. This is crucial in problems with smooth solutions, where improved accuracy per degree of freedom is obtained in comparison with the classical FEM. It explains the wide range of applications solved successfully with IgA approach and its extensions, see for instance [12,15,25,33,44,49,52,60,63,69].

### 1.1. Related work

The literature dealing with the solution of Helmholtz equation with IgA is extensive and recent, see for instance [18,23,24,26,37,61]. In [37] the performance of IgA to solve exterior scattering problems is investigated, using an absorbing boundary condition on a fictitious boundary to truncate the infinite space. It is shown that IgA is a robust approach to reduce the effects of the pollution error and therefore it is a promising tool to solve high frequency acoustic problems. In [18] IgA is used to solve Helmholtz equation with several boundary conditions in 2D regions. The results of a convergence study are presented confirming that IgA outperforms FEM for similar degrees of freedom, specially when the frequency of the waves increases. In [23] the effect of higher continuity of B-spline basis function on the pollution error is studied. The numerical experiments for several basis function degrees  $p$  show that for a given  $p$ , and a fixed number of degrees of freedom, the error drops by an order of magnitude when using IgA compared to FEM. In [24] the Helmholtz equation with Robin boundary condition is tackled using IgA. GMRES method for solving the linear system resulting from IgA is investigated, including the use of preconditioners such as ILU with a complex shift and complex shifted Laplace. The study concludes that, for all wavenumbers, GMRES converges at a fewer iterations with IgA compared to FEM. Moreover, the pollution error is significantly reduced with IgA, even when it is not completely eliminated. In [26], the focus is on the numerical solution of the linear system derived from IgA discretization of Helmholtz equation. The system is solved with GMRES and its convergency is accelerated using a deflation technique, combined with the approximated computation of the inverse of the CSLP with a geometric multigrid method. Numerical results for one, two and three dimensional problems are shown, confirming scalable convergence with respect to the wavenumber and the order of the B-spline basis functions. The recent paper [61] handles acoustic scattering problems using a general PML formulation based on the spline space in which the numerical solution is sought. This enables the PML to be truly matched to any convex and smooth artificial boundary.

For acoustic problems and another engineering applications, several comparisons between IGA and standard FEM have been published confirming the better accuracy of IgA approach and its extensions, see [3,4,12,22,25,38].

Another approach that has been extensively used for approximating the solution of the Helmholtz acoustic equation is the boundary element method (BEM) that, in comparison to FEM, is advantageous since it handles unbounded domains by modeling only the inner boundaries without the introduction of any truncation surfaces (which are sources of truncation errors). BEM can also be coupled with IgA giving rise to the so-called IGABEM. In PhD thesis [49] several Helmholtz acoustic problems are solved with two BEM methods, IGABEM and eXtended isogeometric BEM (XIBEM), obtaining higher accuracy in comparison with standard BEM. IGABEM and XIBEM are used in different engineering and acoustic problems giving very accurate results for frequencies between 50 Hz and 22 kHz. Refs. [13–17,44–46,50–52,56,60,64] provide a good, but not exhaustive, sample of relevant references on IGABEM and XIBEM analysis of acoustics.

In order to reduce the number of degrees of freedom and to achieve higher accuracy on coarser meshes, an approach that is common to conventional FEM, IgA and BEM schemes is to use approximation spaces enriched by a set of wave-like functions depending on the wavenumber. This idea led first to the Partition of Unity Finite Element Method (PUFEM) [41,43], that was combined later with IgA in PUIGA method [22]. The approximation space of IGABEM is enriched in a partition of unity sense in [44–46], where XIBEM is introduced and favorably compared to conventional BEM and IGABEM. The ill-conditioned linear systems are solved with singular value decomposition (SVD) for small-medium frequencies.

In the attempt to capture fine geometric details, the usual tensor product of NURBS may produce an unnecessary increase of computational cost for IgA approach. Some alternatives have been proposed based on unstructured representations, such as T-splines [11], or polynomial splines over hierarchical T-meshes (PHT-splines) [62]. An acoustic IGABEM method based on T-splines is proposed in [57] for problems with low frequency. For problems of time-harmonic acoustics modeled by the Helmholtz equation, some relevant references of these alternative adaptive local refinements may be found in [49].

### 1.2. Our contribution

The main contribution of this paper is the application of IgA approach to the solution of a radiation problem, mathematically modeled with the 2D Helmholtz equation with mixed boundary conditions and very high values of

the wavenumber  $k$ . Details concerning the main steps of IgA method are discussed, with focus on some aspects not covered in available publications. With the open source software GeoPDEs [21] we have implemented an in-house code and by means of a wide experimentation we study different issues of IgA approach. In particular, we show that the quality of the parametrization has a important influence in the precision of  $u^h(x, y)$ , even when the domain has a simple geometry. Moreover, it becomes clear that the error of  $u^h(x, y)$  also depends on the number of B-splines functions. In particular, the number  $m$  of B-splines functions in the wave propagation direction  $y$  is tied up to the noise of the absolute value of  $u^h(x, y)$  restricted to  $y$  axis,  $|u^h(0, y)|$ . On the other hand, the number  $n$  of B-splines functions in the direction  $x$  perpendicular to the wave propagation is related to the phase and amplitude shifts of  $|u^h(0, y)|$ . Furthermore, we show that the matrix obtained from the incomplete (ILU) factorization of the Complex Shifted Laplacian, is a good preconditioner for the linear system derived from IgA discretization of Helmholtz equation with mixed boundary conditions, even when  $k$  is large. Finally, we compare the results of the numerical implementation of IgA with the solutions obtained using classic FEM, for high values of  $k$ . The superiority of the performance of IgA is shown by means of several experiments, which confirm that using less degrees of freedom, IgA provides smoother approximated solutions with a substantially reduced pollution.

## 2. Physical problem and variational formulation

### 2.1. The radiation problem

In this paper we are interested in acoustic wave applications. Under the assumption that the acoustic wave propagation is linear and also that the amplitude of shear waves in the media are much smaller than the amplitude of the pressure waves, nonlinear effects and shear waves may be neglected. In consequence, the acoustic wave pressure is a complex function solution of the Helmholtz equation.

Our problem is inspired by the experiments to measure focused ultrasound induced heating in a tissue phantom [9,58]. In 3D, our simplified problem models an infinite right prism with semicircular basis  $P_S = \{(x, y, z), y \geq 0, x^2 + y^2 \leq r^2\}$  and the transducer is an infinity strip of width  $2a$ ,  $\{(x, 0, z), |x| \leq a\}$ , that emits a pulse of constant amplitude  $C$ . The applied pulse acts in the  $x$ - $y$  plane and does not vary in the  $z$  direction. The volume enclosed by the semicircular right prism  $P_S$  is filled with an homogeneous tissue, thus the wavenumber  $k$  is a positive constant. In this work we consider a simpler 2D plane strain model in the  $x$ - $y$  plane. The physical 2D domain is the semicircle of radius  $r$  and center on the origin of coordinates  $\Omega = \{(x, y), y \geq 0, x^2 + y^2 \leq r^2\}$ . Moreover, a transducer of width  $2a$ , with  $0 < a < r$ , and flat geometry is located at the origin, see Fig. 1. The transducer emits a pulse of high frequency  $f$  of order  $10^6$  Hz, with speed  $c$  and constant amplitude equal to  $C > 0$ . Since  $k = 2\pi f/c$ , for  $c$  of order  $10^3 \text{ m s}^{-1}$  the value of  $k$  is of order  $10^3 \text{ m}^{-1}$ .

Dirichlet boundary condition  $u(x, y) = C$  is imposed on  $\Gamma_D := \{(x, y), |x| \leq a, y = 0\}$ . Additionally, boundary  $\Gamma_N := \{(x, y), a < |x| < r, y = 0\}$  is simulated as an acoustically rigid wall by setting the normal velocity equal to zero. Dirichlet and Neumann boundary conditions are known in the literature as rigid and free baffle respectively.

Finally, it is necessary to require that  $\Gamma_R := \{(x, y), x^2 + y^2 = r^2, y > 0\}$  behaves as a non-reflecting boundary. The simplest approximation of non-reflecting boundary condition is obtained imposing the Robin condition (4) on  $\Gamma_R$ . Robin condition is the first member of the Bayliss–Turkel infinite hierarchy of boundary conditions to simulate outgoing radiation [8]. Robin condition is inexact, and it is specially inaccurate when wave incidence is not perpendicular to  $\Gamma_R$  or when sources are close to  $\Gamma_R$  [7,29]. In our problem we assume that  $a \ll r$  and that  $r$  is such that the number of wave lengths between  $\Gamma_R$  and the transducer is large. Under these assumptions, the wave front impinges  $\Gamma_R$  almost perpendicularly and  $\Gamma_R$  is far away from the source. Thus, for convenience we choose Robin condition as non-reflecting boundary condition, since this approximation is of sufficient accuracy for the application and it is simpler to implement. Better approximations of non-reflecting boundary could be obtained imposing Perfectly Matched Layers (PML) boundary condition [61].

In the rest of the paper we call *radiation problem* to the solution of equation

$$-\Delta u(x, y) - k^2 u(x, y) = 0, \quad (x, y) \in \Omega \tag{1}$$

with *mixed* boundary conditions

$$u(x, y) = C \quad \text{on } \Gamma_D \tag{2}$$

$$\frac{\partial u(x, y)}{\partial \vec{n}} = 0 \quad \text{on } \Gamma_N \tag{3}$$

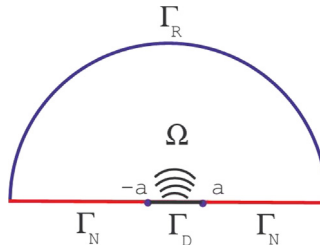


**Fig. 1.** Physical domain of radiation problem. The boundary  $\Gamma$  is subdivided in three curves:  $\Gamma_D, \Gamma_N$  and  $\Gamma_R$ . A transducer of width  $2a$  is located in the origin of coordinates.

$$\frac{\partial u(x, y)}{\partial \vec{n}} + iku(x, y) = 0 \quad \text{on } \Gamma_R \tag{4}$$

where  $\vec{n}$  denotes the normal vector to the boundary  $\Gamma_N$  or  $\Gamma_R$  and  $i$  denotes the imaginary unit.

Near the transducer, in the near field area, there are significant fluctuations in the ultrasound intensity. However, from some point on the pressure waves form a relatively uniform front that spreads out in a pattern originating from the center of the transducer. This area is called the far field and it is important in applications, since optimal detection occur at the start of far field, where the sound wave is well behaved and attains its maximum strength. The near field length  $N_f$  defines the transition point between the near field and the far field. This point, sometimes referred to as the “natural focus”, can be calculated as  $N_f = \frac{a^2}{\lambda}$ , where  $\lambda = \frac{2\pi}{k}$  is the wavelength. In our experiments, we always select  $r \geq 2N_f$  in order to guarantee that  $N_f$  is included in the domain  $\Omega$ . The value of the semi-width  $a$  is fixed by physical considerations, see Sections 4.2.2 and 4.3.2.

### 2.2. Variational formulation

Denote by  $V_0$  the subspace of  $H^1(\Omega)$

$$V_0 = \{v : \Omega \rightarrow \mathbb{C}, v \in H^1(\Omega), v(x, y) = 0 \text{ for } (x, y) \in \Gamma_D\} \tag{5}$$

To obtain the variational formulation, we multiply (1) by  $\bar{v}$ , the complex conjugate of  $v \in V_0$ , integrate on  $\Omega$  and apply Green’s first identity. Denoting by  $\nabla v = \left(\frac{\partial v}{\partial x}, \frac{\partial v}{\partial y}\right)^t$  and taking into account the mixed boundary conditions we arrive to the variational formulation of the radiation problem:

$$\text{Find } u \in H^1(\Omega) \text{ with } u = C \text{ on } \Gamma_D, \text{ such that } a(u, v) = 0 \text{ for all } v \in V_0 \tag{6}$$

where the sesquilinear form  $a(u, v) : H^1(\Omega) \times H^1(\Omega) \rightarrow \mathbb{C}$  is given by,

$$a(u, v) = \int_{\Omega} (\nabla u(x, y)^t \nabla \bar{v}(x, y) - k^2 u(x, y) \bar{v}(x, y)) d\Omega + ik \int_{\Gamma_R} u(x, y) \bar{v}(x, y) d\Gamma_R \tag{7}$$

Assume that the physical domain  $\Omega$  has been parametrized by a function  $\mathbf{F}(\xi, \eta) : \hat{\Omega} \rightarrow \Omega$ , defined on the unit square  $\hat{\Omega}$  and with piecewise smooth inverse. With the help of  $\mathbf{F}(\xi, \eta)$  the double integral in (7) may be transformed into an integral over  $\hat{\Omega}$ . Denote by  $J\mathbf{F}(\xi, \eta)^{-t}$  the transpose of the inverse of the Jacobian matrix of  $\mathbf{F}(\xi, \eta)$ . Then  $a(u, v)$  can be written as,

$$\begin{aligned} a(u, v) &= \int_0^1 \int_0^1 (J\mathbf{F}(\xi, \eta)^{-t} \nabla u(\mathbf{F}(\xi, \eta)))^t (J\mathbf{F}(\xi, \eta)^{-t} \nabla \bar{v}(\mathbf{F}(\xi, \eta))) |\det J\mathbf{F}(\xi, \eta)| d\xi d\eta \\ &\quad - k^2 \int_0^1 \int_0^1 u(\mathbf{F}(\xi, \eta)) \bar{v}(\mathbf{F}(\xi, \eta)) |\det J\mathbf{F}(\xi, \eta)| d\xi d\eta + ik \int_{\Gamma_R} u(x, y) \bar{v}(x, y) d\Gamma_R \end{aligned} \tag{8}$$

To obtain a formulation in  $\hat{\Omega}$  we still have to rewrite the last integral in (8). In Section 3.2 we explain how to construct  $\mathbf{F}(\xi, \eta)$  in such a way that  $\Gamma_D \cup \Gamma_N = \mathbf{F}(\xi, 0)$ ,  $0 \leq \xi \leq 1$ . Moreover, we subdivide  $\Gamma_R$  in three consecutive circular arcs:  $c_l, c_t$  and  $c_r$  and require that

$$\mathbf{F}(0, \eta) = c_l(\eta), \quad 0 \leq \eta \leq 1 \tag{9}$$

$$\mathbf{F}(\xi, 1) = c_t(\xi), \quad 0 \leq \xi \leq 1 \tag{10}$$

$$\mathbf{F}(1, \eta) = c_r(\eta), \quad 0 \leq \eta \leq 1 \tag{11}$$

Taking into account that  $\mathbf{F}(\xi, \eta) = (x(\xi, \eta), y(\xi, \eta))$ , from (9), (10) and (11) we obtain an expression for the integral on  $\Gamma_R$  that only depends on  $\xi$  and  $\eta$ . Substituting this expression in (8) we obtain,

$$\begin{aligned} \alpha(u, v) &= \int_0^1 \int_0^1 \nabla u(\mathbf{F}(\xi, \eta))^t (J\mathbf{F}(\xi, \eta))^t (J\mathbf{F}(\xi, \eta))^{-1} \nabla \bar{v}(\mathbf{F}(\xi, \eta)) |\det J\mathbf{F}(\xi, \eta)| \, d\xi d\eta \\ &\quad - k^2 \int_0^1 \int_0^1 u(\mathbf{F}(\xi, \eta)) \bar{v}(\mathbf{F}(\xi, \eta)) |\det J\mathbf{F}(\xi, \eta)| \, d\xi d\eta + ik \int_0^1 u(\mathbf{F}(0, \eta)) \bar{v}(\mathbf{F}(0, \eta)) \|c'_t(\eta)\|_2 \, d\eta \\ &\quad + ik \int_0^1 u(\mathbf{F}(\xi, 1)) \bar{v}(\mathbf{F}(\xi, 1)) \|c'_t(\xi)\|_2 \, d\xi + ik \int_0^1 u(\mathbf{F}(1, \eta)) \bar{v}(\mathbf{F}(1, \eta)) \|c'_r(\eta)\|_2 \, d\eta \end{aligned} \tag{12}$$

### 3. Galerkin method with isogeometric approach

The Galerkin method solves the variational problem assuming that the approximated solution belongs to a finite-dimensional subspace  $V^h$  of  $V_0$ . In the classical FEM,  $V^h$  consists of piecewise polynomials functions with global  $C^0$  continuity. In the general isogeometric approach [19],  $V^h$  is generated by tensor product NURBS functions with higher global continuity. Moreover, the physical domain  $\Omega$  is also parametrized by a tensor product NURBS function  $\mathbf{F}(\xi, \eta)$ .

#### 3.1. B-splines

For the sake of completeness and also in order to introduce the notation, we present briefly the B-spline functions, which are the core of IgA method. To define B-splines of order  $p$  (degree  $p - 1$ ), we need a nondecreasing knot sequence  $t = \{t_1, t_2, \dots, t_{n+p}\}$ . Using  $t$ , it is possible to construct  $n$  univariate B-splines of order  $p$ , that we denote by  $B_{1,t}^p(\xi), \dots, B_{n,t}^p(\xi)$ . These functions are obtained from Cox–de Boor recursion formula [48],

$$B_{i,t}^p(\xi) = \frac{\xi - t_i}{t_{i+p-1} - t_i} B_{i,t}^{p-1}(\xi) + \frac{t_{i+p} - \xi}{t_{i+p} - t_{i+1}} B_{i+1,t}^{p-1}(\xi) \tag{13}$$

starting with B-splines of order 1,

$$B_{i,t}^1(\xi) = \begin{cases} 1 & \text{for } t_i \leq \xi < t_{i+1} \\ 0 & \text{otherwise} \end{cases}$$

Spline space generated by functions  $B_{i,t}^p$  is denoted by  $\mathbb{S}_{p,t}$ .

Univariate NURBS basic functions of order  $p$  with knots  $t$  are given by,

$$R_{i,t}^p(\xi) = \frac{w_i B_{i,t}^p(\xi)}{\sum_{l=1}^n w_l B_{l,t}^p(\xi)}, \quad i = 1, \dots, n \tag{14}$$

where  $w_i$  are the weights.

In order to define bivariate B-spline functions two nondecreasing knot sequences  $t^\xi = \{t_1^\xi, t_2^\xi, \dots, t_{n+p_1}^\xi\}$  and  $t^\eta = \{t_1^\eta, t_2^\eta, \dots, t_{m+p_2}^\eta\}$  are necessary. In terms of these sequences, tensor product polynomial B-splines of order  $p_1$  and  $p_2$  in  $\xi$  and  $\eta$  directions respectively are defined by,

$$B_{i,j}^{p_1,p_2}(\xi, \eta) := B_{i,t^\xi}^{p_1}(\xi) B_{j,t^\eta}^{p_2}(\eta), \quad i = 1, \dots, n, \quad j = 1, \dots, m \tag{15}$$

As in the univariate case, bivariate NURBS basic functions  $R_{i,j}^{p_1,p_2}$  are defined from polynomial B-splines as,

$$R_{i,j}^{p_1,p_2}(\xi, \eta) := \frac{w_{i,j} B_{i,t^\xi}^{p_1}(\xi) B_{j,t^\eta}^{p_2}(\eta)}{\sum_{l=1}^n \sum_{s=1}^m w_{l,s} B_{l,t^\xi}^{p_1}(\xi) B_{s,t^\eta}^{p_2}(\eta)}, \quad i = 1, \dots, n, \quad j = 1, \dots, m \tag{16}$$

where  $w_{i,j}$  are the weights. To simplify the notation, in the rest of the paper we do not write the subindex  $t^\xi$  or  $t^\eta$  of the B-spline functions when it is clear from the context.

In the next two sections we use quadratic NURBS to parametrize  $\Omega$  and polynomial B-splines to generate the space  $V^h$ . It means that in our IgA approach basis functions for parametrizing the geometry are not the same that

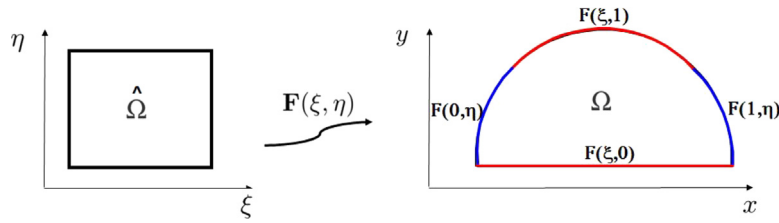


Fig. 2. Parametrization  $F(\xi, \eta)$  mapping  $\hat{\Omega}$  in  $\Omega$ . The semicircle is subdivided in three curves.

those defining the approximation space. This non-isoparametric approach is very useful, since it allows to improve the numerical solution refining locally the approximation space and keeping the same coarser parametrization of the domain.

### 3.2. Parametrization of the domain

The parametrization of the physical domain  $\Omega$  is the first step of IgA approach. In general it is assumed that the map  $F(\xi, \eta)$  parametrizing  $\Omega$  is computed also a NURBS function. In some problems, the boundary  $\Gamma$  of  $\Omega$  is available from CAD systems and the computation of  $F(\xi, \eta)$  is reduced to the parametrization of the interior of  $\Omega$ . Since in our problem the geometry of  $\Omega$  is simple, it is possible to parametrize it with a tensor product NURBS function  $F(\xi, \eta)$ , composed by only one patch and defined on the unit square  $\hat{\Omega}$ .

In order to construct the map  $F(\xi, \eta) = (x(\xi, \eta), y(\xi, \eta))$  we start parametrizing  $\Gamma$ . As we already mentioned the semicircle is subdivided in 3 circular sectors, see Fig. 2, and we denote by  $c_l(\eta)$  and  $c_r(\eta)$ , with  $0 \leq \eta \leq 1$ , the parametrization of the “left” and “right” curves respectively. Moreover, we assume that both curves have the same arc length. The arc of circle defining the “top” curve is represented by  $c_t(\xi)$ , with  $0 \leq \xi \leq 1$  and we denote by  $c_b(\xi)$ ,  $0 \leq \xi \leq 1$  the segment of line passing through the points  $(-r, 0)$  and  $(r, 0)$  and defining the “bottom” curve. Let  $\theta$ ,  $0 < \theta < \pi/2$ , be the angle in the counterclockwise between the positive  $x$  axis and the ray from the origin and the common point between curves  $c_r(\eta)$  and  $c_t(\xi)$ .

It is well known that circular arcs can be written exactly as quadratic NURBS [48], which are piecewise conic curves. In particular, the arc of a circle corresponding to a central angle  $\leq \pi/2$  can be written in terms of a quadratic NURBS composed by an unique conic section. In that case the sequence of knots  $t^\eta$  defining the functions in (14) has not interior knots. Since by hypotheses  $\theta < \pi/2$ , curves  $c_l(\eta)$  and  $c_r(\eta)$  are in this case. For the top curve  $c_t(\xi)$  we consider two possibilities. If  $\theta \geq \pi/4$ , then the central angle corresponding to  $c_t(\xi)$  is less or equal than  $\pi/2$  and  $c_t(\xi)$  is written as linear combination of functions  $R_{i,t^\xi}^3(\xi)$  for a knot sequence  $t^\xi$  with no interior knots. On the other hand, if  $\theta < \pi/4$ , then the central angle corresponding to  $c_t(\xi)$  is greater than  $\pi/2$  and  $c_t(\xi)$  is written in terms of the quadratic NURBS for a sequence of knots  $t^\xi$  with one interior knot. Elevating the degree of  $c_b(\xi)$  [48], this curve can be also represented in terms of functions  $R_{i,t^\xi}^3$ .

Once that  $c_b(\xi)$ ,  $c_t(\xi)$  have been written as quadratic NURBS curves with knots  $t^\xi$  and  $c_l(\eta)$  and  $c_r(\eta)$  have been also written as quadratic NURBS with knots  $t^\eta$ , the map  $F_\theta(\xi, \eta)$  parametrizing  $\Omega$  is defined as the bilinearly blended Coon’s patch interpolating them [48] and given by,

$$F_\theta(\xi, \eta) = \sum_{i=1}^{n_F} \sum_{j=1}^{m_F} \mathbf{P}_{i,j} R_{i,j}^{3,3}(\xi, \eta) \tag{17}$$

where  $\mathbf{P}_{i,j}$  are the control points and  $R_{i,j}^{3,3}(\xi, \eta)$  are the functions (16) for  $p_1 = p_2 = 3$  and knots  $t^\xi$  and  $t^\eta$ . Observe that  $F_\theta(\xi, \eta)$  satisfies the interpolation conditions (9), (10) and (11) and also  $F_\theta(\xi, 0) = c_b(\xi)$ ,  $0 \leq \xi \leq 1$ .

For any  $\theta$  with  $0 < \theta < \pi/2$  the map  $F_\theta(\xi, \eta) : \hat{\Omega} \rightarrow \Omega$  is bijective. Moreover, if  $JF$  denotes the Jacobian matrix of a given map  $F$ , then  $\det JF_\theta(\xi, \eta) > 0$  on  $\hat{\Omega} \setminus \{(0, 1), (1, 1)\}$  and  $\det JF_\theta(0, 1) = \det JF_\theta(1, 1) = 0$ . Other properties of  $F_\theta(\xi, \eta)$  depend on the specific value of parameter  $\theta$ . To illustrate the possible situations consider two parametrizations of  $\Omega$  with  $r = 0.133$ , obtained for  $\theta := \theta_1 = \pi/20$  and for  $\theta := \theta_2 = \pi/4$ . For both parametrizations curves  $c_l(\eta)$ ,  $c_r(\eta)$  are represented as quadratic NURBS curves with knots  $t^\eta = \{0, 0, 0, 1, 1, 1\}$ , hence the number of basic functions in  $\eta$  directions is  $m_F = 3$ . For the parametrization with  $\theta = \theta_1$ , the

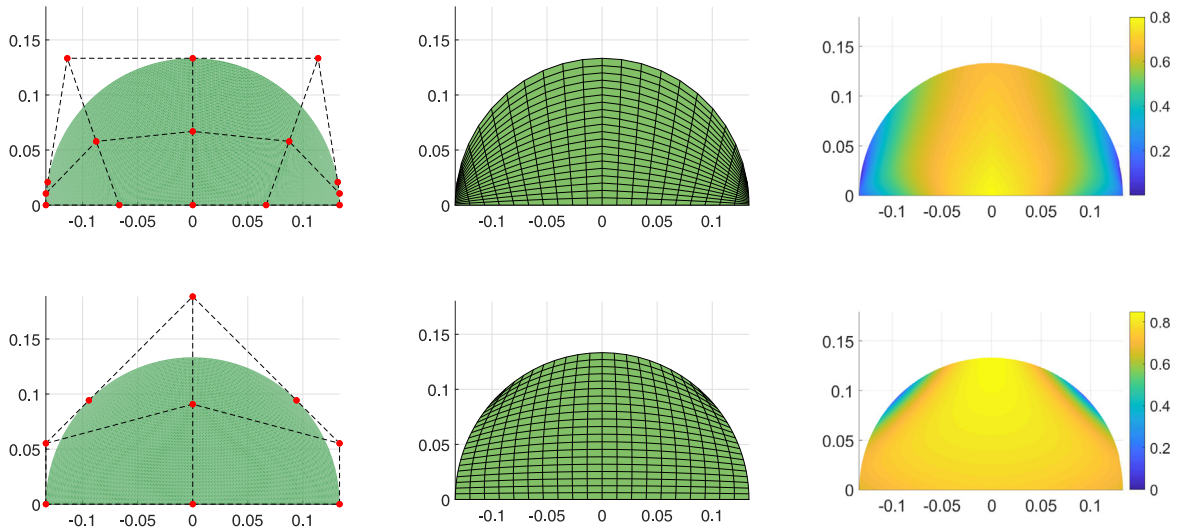


**Fig. 3.** Left: control mesh of the parametrization  $\mathbf{F}_\theta(\xi, \eta)$ , center: quadrilateral mesh obtained as image by  $\mathbf{F}_\theta(\xi, \eta)$  of a rectangular mesh  $\mathcal{Q}$  in  $\hat{\Omega}$ , right: mean ratio Jacobian  $J_r(\xi, \eta)$ . First row correspond to parametrization  $\mathbf{F}_{\theta_1}(\xi, \eta)$  and second row to parametrization  $\mathbf{F}_{\theta_2}(\xi, \eta)$ .

central angle of the top curve  $c_t(\xi)$  is greater than  $\pi/2$  and  $c_t(\xi)$  is represented as a NURBS curve with knots  $t^\xi = \{0, 0, 0, 1/2, 1/2, 1, 1, 1\}$ . The corresponding NURBS space has dimension  $n_F = 5$  and the control mesh of  $\mathbf{F}_\theta$  has 15 control points, see Fig. 3 (left, top). On the other hand, for the parametrization with  $\theta = \theta_2$ , the central angle of the top curve  $c_t(\xi)$  is  $\pi/2$  and  $c_t(\xi)$  is written in terms quadratic NURBS with knots  $t^\xi = \{0, 0, 0, 1, 1, 1\}$ . It means that  $n_F = 3$  and the control mesh of  $\mathbf{F}_\theta(\xi, \eta)$  has in this case 9 points, see Fig. 3 (left, bottom).

The quality of a parametrization  $\mathbf{F}(\xi, \eta)$  of  $\Omega$  influences the precision of the solution computed with isogeometric approach [40]. In this sense, a good uniformity and orthogonality of the isoparametric curves of  $\mathbf{F}(\xi, \eta)$  is desirable. A very popular measure of the quality of the parametrization in the point  $\mathbf{F}(\xi, \eta)$  is the mean ratio Jacobian [39] given by,

$$J_r(\xi, \eta) = \frac{2 \det \mathbf{J}\mathbf{F}(\xi, \eta)}{\|\mathbf{F}_\xi(\xi, \eta)\|_2^2 + \|\mathbf{F}_\eta(\xi, \eta)\|_2^2} \tag{18}$$

where  $\mathbf{F}_\xi(\xi, \eta) = \left(\frac{\partial x}{\partial \xi}, \frac{\partial y}{\partial \xi}\right)$  and  $\mathbf{F}_\eta(\xi, \eta) = \left(\frac{\partial x}{\partial \eta}, \frac{\partial y}{\partial \eta}\right)$  are the tangent vectors to the isoparametric curves and  $\|\cdot\|_2$  denotes the Euclidean norm. If the map  $\mathbf{F}(\xi, \eta)$  is injective, then  $\det \mathbf{J}\mathbf{F}(\xi, \eta)$  does not change sign. Assuming that it is positive it holds that  $0 < J_r(\xi, \eta) \leq 1$ . A value of  $J_r$  equal to 1 at a point  $\mathbf{P}_0 = \mathbf{F}(\xi_0, \eta_0)$  indicates that the isoparametric curves are orthogonal at  $\mathbf{P}_0$  and the map  $\mathbf{F}(\xi, \eta)$  produces the same length distortion at  $\mathbf{P}_0$  in both parametric directions  $\xi$  and  $\eta$ .

In the center of Fig. 3 we show the mesh  $\mathbf{F}_\theta(\mathcal{Q})$  in  $\Omega$  with vertices computed as the image by  $\mathbf{F}_\theta(\xi, \eta)$  of the vertices of a rectangular mesh  $\mathcal{Q}$  in  $\hat{\Omega}$ . Observe that for  $\theta = \pi/4$  (second row and center of Fig. 3) the parametrization  $\mathbf{F}_\theta$  preserves the geometry of the quadrilaterals in  $\mathcal{Q}$  almost everywhere, except in small areas near the two points  $S^- := \mathbf{F}_\theta(0, 1)$  and  $S^+ := \mathbf{F}_\theta(1, 1)$ . Moreover, the vertical isolines of  $\mathbf{F}_\theta$  intersect almost orthogonally the boundary of  $\Omega$  at  $y = 0$ , where Dirichlet and Neumann boundary conditions are defined. On the other hand, for  $\theta = \pi/20$  more deformations are observed in the quadrilaterals of  $\mathbf{F}_\theta(\mathcal{Q})$  (first row and center of Fig. 3). A value of  $\pi/4 \ll \theta < \pi/2$  is not recommended, since in that case the points  $S^-$  and  $S^+$  become too close to the most interesting region  $|x| \leq a$ , where the highest pressure values are located (see Fig. 4 (left)).

On the right of Fig. 3 we show a color map, where colors correspond to the values of  $J_r(\xi, \eta)$  according to (18). A yellow color indicates that  $J_r \geq 0.8$ . Hence, the distortion introduced by the parametrization  $\mathbf{F}_\theta(\xi, \eta)$  for  $\theta = \pi/4$  is small almost everywhere, except on the two blue areas (values of  $J_r$  close to 0.4) near the points  $S^-$  and  $S^+$ , where the distortion is higher. Observe that blue areas are not contained in the interest region  $|x| \leq a$ .

In Section 4.2.1 we show the effect of the parametrization in the accuracy of the solution computed with isogeometric approach. In this sense, the parametrization  $\mathbf{F}_\theta$  with  $\theta = \pi/4$  has the best performance. Since  $\mathbf{F}_{\pi/4}$  is

close to be optimal in the mean ratio Jacobian metric in the region of interest, it is used in the rest of the paper to parametrize  $\Omega$ . Starting from  $\mathbf{F}_{\pi/4}$ , the parametrization could be improved using more sophisticated methods that compute the best parametrization by means of nonlinear optimization [1,67,68]. An analysis-suitable parametrization may be also constructed as an inverse of a bijective mapping from the target domain to the parametric space [53,66]. Another appealing approach is the construction of a high-quality patch-meshing with few singularities, which may be obtained by means of the robust planar partition framework proposed in [65].

### 3.3. Galerkin method with B-spline functions

Galerkin method replaces the infinite dimensional space  $V_0$  by a finite dimensional space  $V^h$ . In this paper  $V^h$  is defined using tensor product B-spline functions (15) and the map given by (17). To simplify the notation in this section we omit the dependence of  $\theta$  of the parametrization and denote it by  $\mathbf{F}(\xi, \eta)$ . Given  $n$  and  $m$ , the knots  $t^\xi$  and  $t^\eta$  are defined by,

$$t^\xi = \left( \overbrace{0, \dots, 0}^{p_1-1 \text{ times}}, \xi_1, \xi_2, \dots, \xi_{n-p_1+2}, \overbrace{1, \dots, 1}^{p_1-1 \text{ times}} \right) \tag{19}$$

$$t^\eta = \left( \overbrace{0, \dots, 0}^{p_2-1 \text{ times}}, \eta_1, \eta_2, \dots, \eta_{m-p_2+2}, \overbrace{1, \dots, 1}^{p_2-1 \text{ times}} \right) \tag{20}$$

where  $0 = \xi_1 < \xi_2 < \dots < \xi_{n-p_1+2} = 1$  are the breakpoints in the direction  $\xi$  and  $0 = \eta_1 < \eta_2 < \dots < \eta_{m-p_2+2} = 1$  are the breakpoints in the direction  $\eta$ . The sequences of breakpoints define a rectangular mesh in  $[0, 1] \times [0, 1]$  with vertices  $(\xi_i, \eta_j)$ ,  $i = 1, \dots, n - p_1 + 2$ ,  $j = 1, \dots, m - p_2 + 2$ .

Functions  $B_{i,j}^{p_1,p_2}$  are a basis of the tensor product space  $\mathbb{S}_{p_1,t^\xi} \otimes \mathbb{S}_{p_2,t^\eta}$ . Due to the assumptions on the parametrization  $\mathbf{F}(\xi, \eta)$ , functions

$$\phi_{i,j}(x, y) = (B_{i,j}^{p_1,p_2} \circ \mathbf{F}^{-1})(x, y), \quad i = 1, \dots, n, \quad j = 1, \dots, m \tag{21}$$

are linearly independent in  $\Omega$ .

#### 3.3.1. IgA approximated solution

Denote by  $V^h$  the space,

$$V^h = \text{span}\{\phi_{i,j}(x, y), \quad i = 1, \dots, n, \quad j = 1, \dots, m\} \tag{22}$$

Galerkin method computes the approximated solution  $u^h(x, y)$  of the variational problem (6) as a function in  $V^h$ . It means that  $u^h(x, y)$  is written as,

$$u^h(x, y) = \sum_{i=1}^n \sum_{j=1}^m \gamma_{i,j} \phi_{i,j}(x, y) \tag{23}$$

for certain unknown coefficients  $\gamma_{i,j} \in \mathbb{C}$ . Denote by  $V_0^h$  the subspace of  $V^h$  constituted by functions in  $V^h$  vanishing on  $\Gamma_D$ ,

$$V_0^h = \text{span}\{\phi_{i,j}(x, y), \quad \text{such that } \phi_{i,j}(x, y) = 0 \text{ for all } (x, y) \in \Gamma_D\} \tag{24}$$

To determine which are the functions  $\phi_{i,j}$  in  $V_0^h$  we have to compute the preimage by  $\mathbf{F}(\xi, \eta)$  of the points  $(-a, 0)$  and  $(a, 0)$  delimiting  $\Gamma_D$ . Since  $\mathbf{F}(\xi, 0)$  with  $0 \leq \xi \leq 1$  is  $\Gamma_D \cup \Gamma_N$ , it is clear that there exist  $\xi_{a^-}$  and  $\xi_{a^+}$  both in  $(0, 1)$  such that,

$$\mathbf{F}(\xi_{a^-}, 0) = (-a, 0), \quad \mathbf{F}(\xi_{a^+}, 0) = (a, 0) \tag{25}$$

Assume that  $\xi_{a^-}$  and  $\xi_{a^+}$  are not already in the knot sequence  $t^\xi$  and it holds:  $t_{i_1}^\xi < \xi_{a^-} < t_{i_1+1}^\xi$  and  $t_{i_2}^\xi < \xi_{a^+} < t_{i_2+1}^\xi$  with  $i_1 \leq i_2$ . Since  $\Gamma_D = \mathbf{F}(\xi, 0)$  with  $\xi_{a^-} \leq \xi \leq \xi_{a^+}$  and  $B_{j,t^\eta}^{p_2}(0) = 0$ , for  $j = 2, \dots, m$ , we conclude that the B-splines not identically null in  $\Gamma_D$  are  $\phi_{i,1}$  for  $i_1 - p_1 + 1 \leq i \leq i_2$  and

$$\phi_{i,1}(x, 0) = B_{i,1}^{p_1,p_2}(\mathbf{F}^{-1}(x, 0)) = B_{i,t^\xi}^{p_1}(\xi) B_{1,t^\eta}^{p_2}(0) = B_{i,t^\xi}^{p_1}(\xi) \tag{26}$$

Hence,

$$V_0^h = \text{span}\{\phi_{i,j}(x, y), \quad 1 \leq i \leq n, \quad 2 \leq j \leq m, \quad \text{and} \quad \phi_{i,1}(x, y), \quad i \notin [i_1 - p_1 + 1, i_2]\} \tag{27}$$

In order to obtain a system of linear equations for the unknowns  $\gamma_{i,j}$  it is convenient to vectorize the basis functions and the corresponding coefficients in (23) introducing the change of indices

$$q = q(i, j) := n(j - 1) + i, \quad i = 1, \dots, n, \quad j = 1, \dots, m \tag{28}$$

With this transformation we rewrite the expression (23) as

$$u^h(x, y) = \sum_{q=1}^N \alpha_q \psi_q(x, y) \tag{29}$$

where  $N := nm$  and

$$\boldsymbol{\alpha} := (\alpha_1, \dots, \alpha_N) = (\gamma_{1,1}, \dots, \gamma_{n,1}, \dots, \gamma_{1,m}, \dots, \gamma_{n,m}) \tag{30}$$

$$(\psi_1(x, y), \dots, \psi_N(x, y)) = (\phi_{1,1}(x, y), \dots, \phi_{n,1}(x, y), \dots, \phi_{1,m}(x, y), \dots, \phi_{n,m}(x, y)) \tag{31}$$

Thus, in the new notation  $V^h = \text{span}\{\psi_q(x, y), \quad q = 1, \dots, N\}$ . Denote by  $I_0$  the set containing the global indices, computed using (28), of functions on  $V_0^h$ . Then  $\psi_q(x, y) = 0$  for  $(x, y) \in \Gamma_D$  and  $q \in I_0$ . In other words,  $V_0^h = \text{span}\{\psi_q(x, y), \quad q \in I_0\}$  and  $\dim(V_0^h) = n_0$ , where  $n_0$  is the size of  $I_0$ . Similarly, denote by  $I_g$  the set of global indices of functions  $\phi_{i,1}(x, y)$  with  $i_1 - p_1 + 1 \leq i \leq i_2$  and let  $n_g$  be the size of  $I_g$ . With this notation  $n_0 + n_g = N$  and  $u^h(x, y)$  can be written as

$$u^h(x, y) = u_0^h(x, y) + u_g^h(x, y) \tag{32}$$

where  $u_0^h(x, y) = \sum_{q \in I_0} \alpha_q \psi_q(x, y)$  and  $u_g^h(x, y) = \sum_{q \in I_g} \alpha_q \psi_q(x, y)$ . Observe that function  $u_0^h(x, y) \in V_0^h$ . Hence, to obtain the Galerkin formulation we substitute in  $\mathbf{a}(u, v) = 0$ , with  $\mathbf{a}(u, v)$  given by (12),  $u$  by  $u^h(x, y)$  defined by (29) and  $v$  by a basis function  $\psi_r(x, y)$ ,  $r \in I_0$  of  $V_0^h$ . The result is,

$$\sum_{q=1}^N \alpha_q (s_{r,q} - k^2 m_{r,q} + i k e_{r,q}) = 0 \quad r \in I_0 \tag{33}$$

where (omitting the dependence of functions of  $(\xi, \eta)$  when it is clear)

$$s_{r,q} = \int_0^1 \int_0^1 (\nabla \psi_q)^t (\mathbf{J}\mathbf{F}^t \mathbf{J}\mathbf{F})^{-1} \nabla \psi_r \, |\det \mathbf{J}\mathbf{F}| \, d\xi d\eta \tag{34}$$

$$m_{r,q} = \int_0^1 \int_0^1 \psi_q \psi_r \, |\det \mathbf{J}\mathbf{F}| \, d\xi d\eta \tag{35}$$

$$e_{r,q} = \int_0^1 \psi_q(\mathbf{F}(0, \eta)) \psi_r(\mathbf{F}(0, \eta)) \|c'_l(\eta)\|_2 \, d\eta + \int_0^1 \psi_q(\mathbf{F}(\xi, 1)) \psi_r(\mathbf{F}(\xi, 1)) \|c'_l(\xi)\|_2 \, d\xi + \int_0^1 \psi_q(\mathbf{F}(1, \eta)) \psi_r(\mathbf{F}(1, \eta)) \|c'_r(\eta)\|_2 \, d\eta \tag{36}$$

Finally we have to impose the Dirichlet boundary condition on  $\Gamma_D$ . For that we fix

$$\alpha_q = C, \quad q \in I_g \tag{37}$$

Let  $(\tilde{x}, 0)$ , with  $-a \leq \tilde{x} \leq a$ , be a point in  $\Gamma_D$ . Then, from (32) we get,

$$u^h(\tilde{x}, 0) = u_0^h(\tilde{x}, 0) + u_g^h(\tilde{x}, 0) = 0 + \sum_{q \in I_g} \alpha_q \psi_q(\tilde{x}, 0) = C \sum_{q \in I_g} \psi_q(\tilde{x}, 0) \tag{38}$$

By construction,  $\mathbf{F}(\xi, \eta)$  maps the boundaries of the unit square on the boundaries of  $\Omega$ . Hence, from (25) we know that there exists  $\tilde{\xi}$  such that  $\mathbf{F}(\tilde{\xi}, 0) = (\tilde{x}, 0)$  with,

$$t_{i_1}^\xi < \xi_{a^-} \leq \tilde{\xi} \leq \xi_{a^+} < t_{i_2+1}^\xi \tag{39}$$

Since  $I_g$  is the set of global indices of functions  $\phi_{i,1}(x, y)$ , with  $i_1 - p_1 + 1 \leq i \leq i_2$ , from (26) and (38) we obtain,

$$u^h(\tilde{x}, 0) = C \sum_{i=i_1-p_1+1}^{i_2} \phi_{i,1}(\tilde{x}, 0) = C \sum_{i=i_1-p_1+1}^{i_2} B_{i,t^\xi}^{p_1}(\tilde{\xi}) \tag{40}$$

But taking into account (39) it is clear that functions  $B_{i,t^\xi}^{p_1}$  vanish in  $\tilde{\xi}$ , for  $i \leq i_1 - p_1$  and for  $i \geq i_2 + 1$ . Hence, (40) can be rewritten as,

$$u^h(\tilde{x}, 0) = C \sum_{i=1}^n B_{i,t^\xi}^{p_1}(\tilde{\xi}) = C$$

where the last equality holds because the B-splines satisfy the unit partition property. Summarizing, with the selection (37) Dirichlet boundary condition holds exactly.

Without loss of generality, assume that unknowns  $\alpha_q$ ,  $q = 1, \dots, N$  have been reorganized in such a way that the first  $n_0$  unknowns correspond to indexes in  $I_0$  and the last  $n_g$  unknowns correspond to indexes in  $I_g$ . Then, taking into account (37) the linear equations (33) can be written as,

$$\sum_{q=1}^{n_0} \alpha_q a_{r,q} = -C \sum_{q=n_0+1}^N a_{r,q} \quad r = 1, \dots, n_0 \tag{41}$$

where  $a_{r,q} = s_{r,q} - k^2 m_{r,q} + ik e_{r,q}$ . In the literature matrices  $S = (s_{r,q})$  and  $M = (m_{r,q})$  for  $r, q = 1, \dots, n_0$  are known as stiffness matrix and mass matrix respectively. Let  $\tilde{\alpha} = (\alpha_1, \dots, \alpha_{n_0})$ , then system (41) can be written in matrix form as,

$$A \tilde{\alpha} = b \tag{42}$$

where  $b = (b_r) = -C \sum_{q=n_0+1}^N a_{r,q}$  for  $r = 1, \dots, n_0$  and  $A = (a_{r,q})$ ,  $r, q = 1, \dots, n_0$  is given by

$$A = S - k^2 M + ik E \tag{43}$$

with  $E = (e_{r,q})$ ,  $r, q = 1, \dots, n_0$ .

**Remarks.**

1. From (42) it is clear than the actual number  $n_0 = N - n_g$  of free parameters of our solution is slightly smaller than the dimension  $N = nm$  of the approximation space  $\mathbb{S}_{p_1,t^\xi} \otimes \mathbb{S}_{p_2,t^\eta}$ . Nevertheless, in the rest of the work we refer to  $N$  as the total number of degrees of freedom.
2. Enforcing exact Dirichlet conditions on  $[-a, a]$ , some basic functions  $\psi_q$  with support that contains points in  $[-a, a]$  and outside of  $[-a, a]$  have prescribed coefficients  $\alpha_q = C$ . This deteriorates the satisfaction of Neumann condition near  $\pm a$ . In order to mitigate this effect it is convenient that the sequence  $t^\xi$  includes knots close to  $\xi_{a^-}$  from the left and knots close to  $\xi_{a^+}$  from the right. In particular, it is recommendable to include the points  $\xi_{a^-}$  and  $\xi_{a^+}$  in  $t^\xi$ . Observe that if  $\xi_{a^-} = t_{i_1}^\xi$  and  $\xi_{a^+} = t_{i_2}^\xi$  then  $I_g$  is the set of global indices of functions  $\phi_{i,1}(x, y)$  with  $i_1 - p_1 + 1 \leq i \leq i_2 - 1$ . The knot sequences  $t^\xi$  of the experiments in Section 4.3 are constructed including the points  $\xi_{a^-}$  and  $\xi_{a^+}$  in  $t^\xi$ .

3.3.2. The dimension of IgA approximation space

In this work we are interested in applications where the frequency  $f$  is near or greater than 1 MHz. Hence, the wavelength  $\lambda$  is of order  $10^{-3}$  m, which means that the solution  $u(x, y)$  is highly oscillatory. To face this problem classic FEM uses a mesh of size  $h_{FEM}$ , with  $h_{FEM} \leq \frac{\lambda}{10}$ , resulting in a high number  $N_{FEM}$  of degrees of freedom.

IgA does not require the construction of a mesh in the physical domain  $\Omega$ . But taking into account that a parametrization  $\mathbf{F}(\xi, \eta)$  of  $\Omega$  is available, it is possible to define a mesh in  $\Omega$  as follows. Associated with B-splines breakpoints  $\xi_i$ ,  $i = 1, \dots, n - p_1 + 2$  and  $\eta_j$ ,  $j = 1, \dots, m - p_2 + 1$ , in directions  $\xi$  and  $\eta$  respectively, there is a mesh  $\mathcal{Q}$  in  $[0, 1] \times [0, 1]$  composed by rectangular elements  $[\xi_i, \xi_{i+1}] \times [\eta_j, \eta_{j+1}]$ . Computing the image by  $\mathbf{F}(\xi, \eta)$  of the points  $(\xi_i, \eta_j)$ , we define a quadrilateral mesh  $\mathcal{K}$  in  $\Omega$ . The vertices of elements in  $\mathcal{K}$  are the points  $\mathbf{F}(\xi_i, \eta_j)$ . Moreover, two vertices in  $\mathcal{K}$  are joined by an edge, if their pre-images are the extreme points of an edge in  $\mathcal{Q}$ . We denote by  $h_{IgA}$  the size of the mesh  $\mathcal{K}$ .

From the previous definition it is clear that  $h_{IgA}$  depends on the selection of the values of  $n$  and  $m$ , that is the dimensions of spline spaces  $\mathbb{S}_{p_1,t^\xi}$  and  $\mathbb{S}_{p_2,t^\eta}$  respectively. In Section 4.3.1 we show through several experiments, that in order to obtain a high accuracy IgA solution, it is enough to select  $n$  and  $m$  in such a way that  $h_{IgA} \leq \frac{\lambda}{6}$ . Moreover, studying the behavior of  $|u^h(0, y)|$ , we show in Section 4.2.3 that  $n$  and  $m$  play different roles in the quality of the approximation computed with  $nm$  degrees of freedom.

### 3.4. On the linear system obtained from IgA discretization

For large values of  $k$ , the numerical solution of the linear system (42) is a challenge. First,  $A$  is very large, since  $u(x, y)$  is highly oscillatory and therefore many degrees of freedom  $N$  are necessary to obtain accurate approximations. Moreover,  $A$  is sparse but it gets denser if we increase the order of B-splines.

In consequence, direct solvers are prohibitively expensive and it is necessary to appeal to iterative solvers. Furthermore, for medium to large values of  $k$ ,  $A$  happens to be indefinite.

Since the convergence rate of iterative methods strongly depends on the condition number  $\kappa(A)$  of matrix  $A$ , it is important to obtain bounds for  $\kappa(A)$  as a function of the mesh size and also as function of the order of B-splines. In [30] bounds for the condition number of the stiffness and mass matrices of IgA discretizations of elliptic PDE are obtained. In general, it is shown that their condition numbers grow quickly with the inverse of mesh size and the polynomial degree  $p$ .

Thus, the matrix  $A$  in (43) is in general ill conditioned and the convergence of a Krylov subspace methods, like GMRES, requires a previous preconditioning of  $A$ . One of the most successful preconditioners, introduced in FEM context in [27], is the Complex Shifted Laplacian (CSLP). It depends on a parameter  $\beta > 0$  and it is given by

$$A_\beta = A + i\beta k^2 M \tag{44}$$

where  $M$  is the mass matrix. It is known [31] that the Shifted Laplacian (44) is a good preconditioner for FEM discretization (in the sense that  $\|I - A_\beta^{-1}A\|$  is small) if  $\beta k$  is of order  $\leq k$ .

Since near-zero eigenvalues hamper the convergence of Krylov subspace methods, it is important to study the spectrum of the preconditioned matrix  $A_\beta^{-1}A$ . In the next Proposition we show some properties of the matrices arising from IgA approach of Galerkin method applied to Helmholtz equation (1) with mixed boundary conditions (2)–(4). Moreover, we show that the eigenvalues of  $A_\beta^{-1}A$  are located on or inside a circle in the complex plane that passes through the origin.

**Proposition 1.** *If  $A, S, E$  and  $M$  are the matrices given in (43) arising from the isogeometric approach of Galerkin method applied to Helmholtz equation (1) with mixed boundary conditions (2)–(4), then it holds*

- (1)  $S$  and  $E$  are symmetric positive semi-definite real matrices. Moreover,  $M$  is a symmetric positive definite real matrix.
- (2)  $A$  is a symmetric, and non Hermitian matrix.
- (3) For all  $\beta > 0$ , the eigenvalues of the preconditioned matrix  $A_\beta^{-1}A$ , with  $A_\beta$  given by (44), are inside or on the circle in the complex plane with center  $c_0 = (\frac{1}{2}, 0)$  and radius  $r_0 = \frac{1}{2}$ .

**Proof.** For  $u, v \in V_0$ , let us consider the following sesquilinear forms,

$$a_S(u, v) = \int \int_\Omega \nabla u^t \nabla \bar{v} \, d\Omega, \quad a_M(u, v) = \int \int_\Omega u \bar{v} \, d\Omega, \quad a_R(u, v) = \int_{\Gamma_R} u \bar{v} \, d\Gamma_R$$

Let  $u^h \in V_0^h \subset V_0$  be different from 0. Then,  $u^h = \sum_{q=1}^{n_0} \alpha_q \psi_q(x, y)$  with  $\alpha_q \in \mathbb{C}$ . Hence,  $a_S(u^h, u^h) = \|\nabla u^h\|_{L^2(\Omega)}^2 \geq 0$ . Since  $a_S(u, v)$  is sesquilinear, we obtain from (34)

$$\begin{aligned} 0 \leq a_S(u^h, u^h) &= a_S \left( \sum_{q=1}^{n_0} \alpha_q \psi_q(x, y), \sum_{r=1}^{n_0} \alpha_r \psi_r(x, y) \right) = \sum_{q=1}^{n_0} \sum_{r=1}^{n_0} \alpha_q \bar{\alpha}_r \int \int_\Omega \nabla \psi_r(x, y)^t \nabla \psi_q(x, y) \, d\Omega \\ &= \sum_{q=1}^{n_0} \sum_{r=1}^{n_0} \alpha_q \bar{\alpha}_r \int_0^1 \int_0^1 (J\mathbf{F}^{-t} \nabla \psi_r(x, y))^t (J\mathbf{F}^{-t} \nabla \psi_q(x, y)) |det J\mathbf{F}| \, d\xi \, d\eta \end{aligned}$$

Hence,

$$0 \leq a_S(u^h, u^h) = (\bar{\alpha}_1, \dots, \bar{\alpha}_{n_0}) S (\alpha_1, \dots, \alpha_{n_0})^t$$

From the last inequality,  $S$  is a  $n_0 \times n_0$  symmetric positive semi-definite real matrix. On the other hand, for  $u^h \in V_0^h \subset V_0$  different from 0, it holds  $0 < \|u^h\|_{L^2(\Omega)}^2 = \int \int_{\Omega} u^h \bar{u}^h d\Omega = a_M(u^h, u^h)$ . Thus, according to (35) we obtain,

$$0 < a_M(u^h, u^h) = \sum_{q=1}^{n_0} \sum_{r=1}^{n_0} \alpha_q \bar{\alpha}_r \int_0^1 \int_0^1 \psi_r(x, y) \psi_q(x, y) |det J\mathbf{F}| d\xi d\eta = (\bar{\alpha}_1, \dots, \bar{\alpha}_{n_0}) M (\alpha_1, \dots, \alpha_{n_0})^t$$

which means that  $M$  is a  $n_0 \times n_0$  symmetric positive definite real matrix. Finally, recalling that a function  $u^h \in V_0^h \subset V_0$  different from 0 may vanish on  $\Gamma_R$ , from (36) we obtain,

$$0 \leq \int_{\Gamma_R} u^h \bar{u}^h d\Gamma_R = a_R(u^h, u^h) = \sum_{q=1}^{n_0} \sum_{r=1}^{n_0} \alpha_q \bar{\alpha}_r e_{r,q} = (\bar{\alpha}_1, \dots, \bar{\alpha}_{n_0}) E (\alpha_1, \dots, \alpha_{n_0})^t$$

Hence,  $E$  is a  $n_0 \times n_0$  symmetric positive semi-definite real matrix. This finishes the proof of (1).

To prove (2), we observe that  $S, M$  and  $E$  are real symmetric matrices. Hence, from (43) and for  $k > 0$  it holds  $A - \bar{A}^t = 2ikE \neq 0$ , thus  $A$  is not Hermitian.

The proof of (3) is based on Theorem 3.5 in [59]. Set  $\mathcal{L} = S, \mathcal{C} = kE$  and  $\mathcal{M} = \frac{1}{c^2} M$ . Then, clearly  $\mathcal{L}$  and  $\mathcal{C}$  are symmetric positive semi-definite real matrices and  $\mathcal{M}$  is a symmetric positive definite real matrix. Moreover, using (43) and (44) we can write,

$$\begin{aligned} A &= S + ikE - k^2M = \mathcal{L} + i\mathcal{C} - z_1\mathcal{M} \\ A_\beta &= S + ikE - k^2(1 - i\beta)M = \mathcal{L} + i\mathcal{C} - z_2\mathcal{M} \end{aligned}$$

with  $z_1 = k^2c^2$  and  $z_2 = (1 - i\beta)k^2c^2$ . Since  $\beta_2 := \Im m(z_2) = -\beta k^2c^2 < 0$ , the hypothesis of Theorem 3.5 in [59] is fulfilled. Hence, the eigenvalues of  $A_\beta^{-1}A$  are inside or on the circle in the complex plane with center  $c_0 = \frac{z_1 - \bar{z}_2}{z_2 - \bar{z}_2} = \frac{1}{2}$  and radius  $r_0 = \left| \frac{z_2 - z_1}{z_2 - \bar{z}_2} \right| = \frac{1}{2}$ . ■

In order to reduce the computational cost and the memory requirements, CSLP matrix (44) is approximated in practice by  $\tilde{A}_\beta = L \cdot U$ , where  $L, U$  are the matrices resulting from ILU factorization (with threshold and pivoting) of  $A_\beta$ . The drop tolerance  $\varepsilon$  of the incomplete LU factorization controls the accuracy of  $\tilde{A}_\beta$  as approximation of  $A_\beta$ . The smaller  $\varepsilon$  the better is the approximation  $\tilde{A}_\beta$ , but at a higher computational cost. The preconditioned system

$$\tilde{A}_\beta^{-1} A \tilde{\alpha} = \tilde{A}_\beta^{-1} b \tag{45}$$

is solved calling to GMRES, and passing as argument the name of a function that uses the factors  $L$  and  $U$  previously computed. In Section 4.2.2 we make several experiments to select free parameters:  $\beta$  for CSLP and  $\varepsilon$  of ILU factorization. Moreover, we fix the maximum number of GMRES iterations and the tolerance for the relative residual.

### 4. Numerical results and discussion

To solve the radiation problem, we have implemented IgA approach in an in-house code, using the open source package **GeoPDEs** [21] to compute the matrix and the right hand side of the linear system (42). IgA results reported here were obtained in a PC with i7-8565U processor, CPU @ 1.80 GHz and 8 Gb of RAM. In our simulations of acoustic radiation, the Dirichlet constant in (2) is  $C = 1$  and the sound propagation speed is  $c = 1500 \text{ m s}^{-1}$ . We compute  $\lambda = \frac{c}{f}$ , and  $k = 2\pi/\lambda$ .

#### 4.1. Simulation of acoustic radiation for a typical problem

In this section we solve a model radiation problem, assuming that the transducer emits a pulse of frequency  $f = 1.0 \text{ MHz}$ , hence  $k = 4188.8 \text{ m}^{-1}$ . The semi-width is  $a = 0.01 \text{ m}$  and  $r = 2N_f = 0.133 \text{ m}$ . The radiation problem is solved with bicubic B-splines, i.e  $p_1 = p_2 = 4$ . Moreover, we choose  $n = 1000$  and  $m = 600$  and

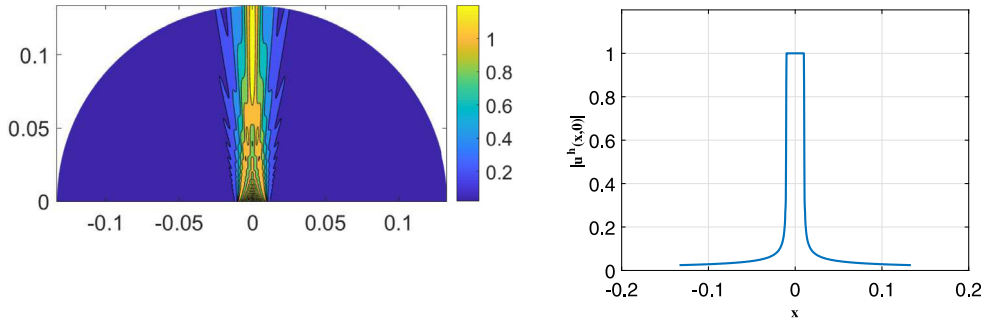


**Fig. 4.** Left: 2D view of function  $|u^h(x, y)|$  for  $f = 1.0$  MHz computed with bicubic B-splines with uniform knots and  $N = 600\,000$  dof ( $n = 1000, m = 600$ ). Right: Graph of the function  $|u^h(x, 0)|$ .

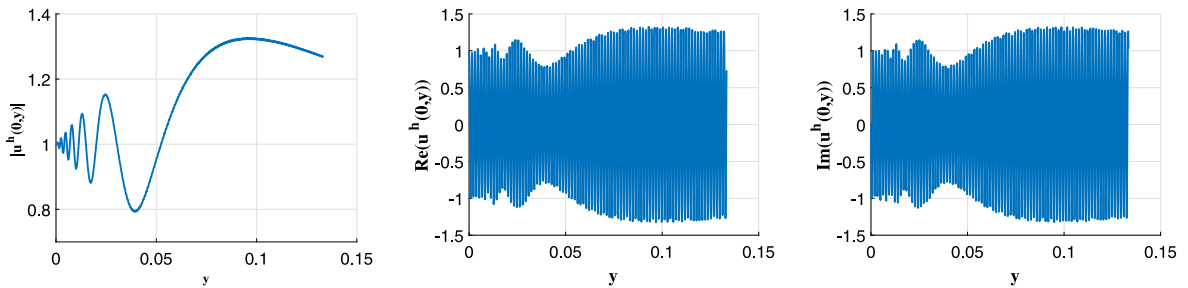


**Fig. 5.** Graphs of the functions  $|u^h(0, y)|, \Re(u^h(0, y))$  and  $\Im(u^h(0, y))$  for  $f = 1.0$  MHz, computed with bicubic B-splines with uniform knots and  $N = 600\,000$  dof ( $n = 1000, m = 600$ ).

uniform knot sequences  $t^\xi$  and  $t^\eta$  in the directions  $\xi$  and  $\eta$  respectively. Hence, the total number of degrees of freedom (*dof*) is  $N = nm = 600\,000$ . The parametrization  $\mathbf{F}_\theta(\xi, \eta)$  is computed as described in Section 3.2 for the parameter  $\theta = \pi/4$ . The preconditioned linear system (45) is solved with GMRES with matrix  $\tilde{A}_\beta$  obtained from ILU factorization of  $A_\beta$  with  $\beta = 0.5$ . More details about the parameters for GMRES convergence are given in Section 4.2.2.

In Fig. 4 (left), we show a 2D view of the function

$$|u^h(x, y)| = ((\Re u^h(x, y))^2 + (\Im u^h(x, y))^2)^{\frac{1}{2}} \tag{46}$$

Colors in this figure indicate that most oscillations of acoustic pressure are in the strip  $-a \leq x \leq a$ . Moreover, the region of the highest acoustic pressure has an elliptical shape and it is located after the natural focus  $N_f = 0.066$  m. In Fig. 4 (right) we show the function  $|u^h(x, 0)|$  for  $-r \leq x \leq r$ . Observe that Dirichlet boundary condition holds in the interval  $[-a, a]$ , while in the rest of the line  $y = 0$  the function  $|u^h(x, 0)|$  is smooth. The behavior of the function  $|u^h(0, y)|$  is shown in Fig. 5, where we also include the graphs of the highly oscillatory functions  $\Re(u^h(0, y))$  and  $\Im(u^h(0, y))$ .

#### 4.2. Discussion about the IgA approach

The practical implementation of IgA approach requires a careful selection of the degree and knots of B-spline functions in each parametric direction, the number of degrees of freedom, the parametrization  $\mathbf{F}(\xi, \eta)$  of the physical domain  $\Omega$  and the numerical solver for the linear equations derived from the discretization. In this section we study the influence of these aspects in the quality and accuracy of the approximated solution  $u^h(x, y)$  computed by IgA approach. In all the experiments of this section we use bicubic B-splines with uniform knots  $t^\xi$  and  $t^\eta$ .

##### 4.2.1. Influence of the parametrization

To examine the effect of the parametrization in the numerical solution  $u^h(x, y)$  we solve again the model problem considered in the previous section (with  $k = 4\,188.8 \text{ m}^{-1}, a = 0.01 \text{ m}$  and  $r = 0.133 \text{ m}$ ), using two parametrizations

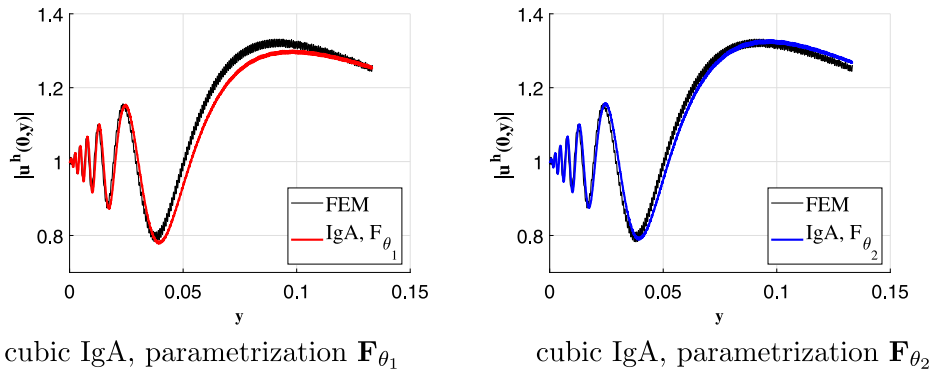


**Fig. 6.** Graph of the function  $|u^h(0, y)|$  for frequency  $f = 1.0\text{MHz}$ , computed with bicubic B-splines with uniform knots. Left: parametrization  $\mathbf{F}_{\theta_1}$  (red), right: parametrization  $\mathbf{F}_{\theta_2}$  (blue). In black the graph of  $|u^h(0, y)|$  computed with FEM. The total number of degrees of freedom is  $N_{IgA} = 500\,000$  and  $N_{FEM} = 3\,330\,886$ . (For interpretation of the references to color in this figure legend, the reader is referred to the web version of this article.)

of  $\Omega$ . More precisely, we consider the parametrizations  $\mathbf{F}_{\theta_1}(\xi, \eta)$  and  $\mathbf{F}_{\theta_2}(\xi, \eta)$  of  $\Omega$  described in Section 3.2 for the parameters  $\theta_1 = \pi/20$  and  $\theta_2 = \pi/4$  respectively. In both cases we study the behavior of the function  $|u^h(x, y)|$  given by (46). Since the maximum amplitude of the acoustic wave pressure is attained on the profile  $x = 0$  in the next experiments we only plot  $|u^h(0, y)|$ .

Fig. 6 shows in color the graphic of  $|u^h(0, y)|$ , computed with bicubic B-spline functions with uniform knots,  $n = 1000$ ,  $m = 500$ , and parametrizations  $\mathbf{F}_{\theta_1}(\xi, \eta)$  (left) and  $\mathbf{F}_{\theta_2}(\xi, \eta)$  (right). For comparison, we also show in black the function  $|u^h(0, y)|$  computed in COMSOL [2] with FEM, using cubic Lagrange polynomials. The numbers  $N_{FEM}$  and  $N_{IgA}$  of degrees of freedom for FEM and IgA approximations are respectively  $N_{IgA} = 500\,000$  and  $N_{FEM} = 3\,330\,886$ . Observe that in the experiments  $N_{IgA}$  is the same for parametrizations  $\mathbf{F}_{\theta_1}(\xi, \eta)$  and  $\mathbf{F}_{\theta_2}(\xi, \eta)$ . From the comparison with FEM solutions it is easy to realize that IgA function  $|u^h(0, y)|$  obtained from the parametrization  $\mathbf{F}_{\theta_2}(\xi, \eta)$  is closer to FEM, than those obtained from parametrization  $\mathbf{F}_{\theta_1}(\xi, \eta)$ .

From similar experiments with parametrizations computed for several values of  $\theta$ , we conclude that the quality of the parametrization has a strong influence in the precision of the approximated solution computed with IgA. In particular, we have observed that for the class of parametrizations  $\mathbf{F}_{\theta}(\xi, \eta)$  constructed in Section 3.2, depending on the parameter  $\theta$ , the best results are obtained when  $\theta = \pi/4$ . In other words, for a fixed number  $N_{IgA}$  of degrees of freedom, the function  $|u^h(0, y)|$  computed with IgA approach using the parametrization  $\mathbf{F}_{\pi/4}(\xi, \eta)$  is an excellent approximation of the function  $|u(0, y)|$ , assuming that  $N_{IgA}$  is large enough.

#### 4.2.2. Performance of GMRES with ILU factorization of CSLP

In this section we perform several numerical experiments to choose suitable values for the parameters  $\beta$  and  $\varepsilon$ , necessary to define the preconditioner  $\tilde{A}_{\beta}$  in (45). We solve the radiation problem always with Dirichlet constant  $C = 1$ , and for relatively low frequencies since we want to compute some eigenvalues of  $A_{\beta}^{-1}A$ . For these frequencies, the semi-width  $a$  is fixed as  $a = 2.5\lambda = 5\pi/(2k)$  and the radius  $r$  is equal to  $r = 2.5 N_f = 2.5 \left(\frac{a^2 k}{2\pi}\right) = 2\pi(2.5)^3/k$ . Hence, the area of  $\Omega$  is inversely proportional to  $k^2$ . The frequencies  $f$  and the corresponding values of  $k$ , as well as  $a$  and  $r$  are contained in Table 1, for problems considered in the experiments. To compute IgA solution we use bicubic B-splines with uniform knots. In Table 1 we also report the values of the IgA input parameters  $n$  and  $m$  and also the mesh size  $h_{IgA}$  as function of the wavelength  $\lambda$ . Note that as  $f$  increases,  $k$  also increases, therefore the solution  $u(x, y)$  is more oscillating and more degrees of freedom  $N$  are necessary to obtain good approximations of  $u(x, y)$ , even when the area of  $\Omega$  is reduced.

In our experiments we always solve the linear systems with GMRES restarting every 30 iterations; the maximum number of iterations is fixed to 6000 and the tolerance for the relative residual is fixed to  $10^{-6}$ .

As we already mentioned, near-zero eigenvalues make difficult the convergence of a Krylov subspace method like GMRES. Hence, it is important to study the spectrum of the preconditioned matrix  $A_{\beta}^{-1}A$ , that depends on the value of  $\beta$ . In the next experiments we consider two values of  $\beta$ , which are independent of  $k$ ,  $\beta = 0.1$  and  $\beta = 0.5$ .

**Table 1**  
Data for IgA solution of the radiation problem.

$f$ (MHz)	$k$ ( $m^{-1}$ )	$a$ (m)	$r$ (m)	$N$	$h_{IgA}$ (m)
0.10	418.9	0.0375	0.234	30 000 ( $n = 200, m = 150$ )	$\lambda/6.18$
0.30	1 256.6	0.0125	0.078	37 400 ( $n = 220, m = 170$ )	$\lambda/6.81$
0.50	2 094.4	0.0075	0.047	50 000 ( $n = 250, m = 200$ )	$\lambda/7.75$

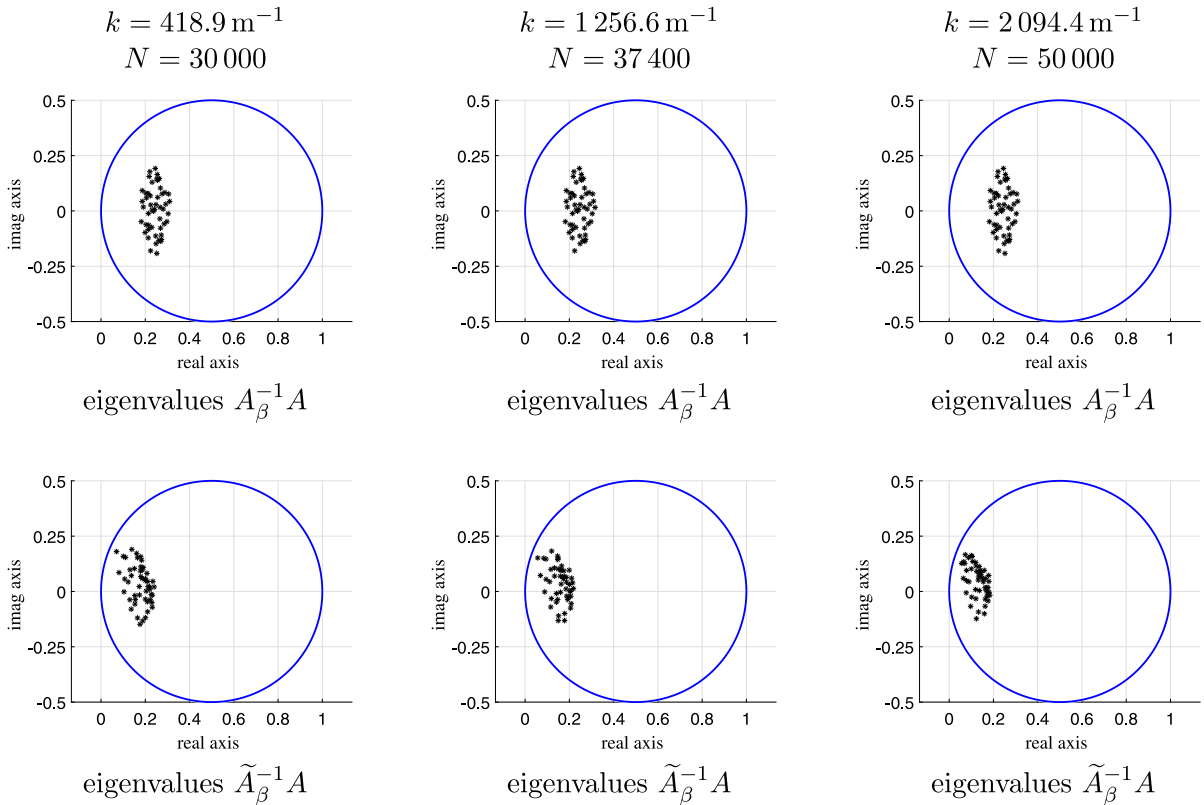


**Fig. 7.** First row: 50 smallest eigenvalues of  $A_\beta^{-1}A$  with  $\beta = 0.1$ . Second row: 50 smallest eigenvalues of  $\tilde{A}_\beta^{-1}A$ , matrix  $\tilde{A}_\beta$  computed with  $\beta = 0.1$  and  $\varepsilon = 10^{-2}$ . Each column corresponds to a problem in Table 1.

In the first row of Fig. 7 we show the (50) smallest in magnitude eigenvalues of  $A_\beta^{-1}A$ , for  $\beta = 0.1$  and for data considered in Table 1. Observe that as theory predicts (see Proposition 1), all the eigenvalues are inside the circle in the complex plane with center  $(\frac{1}{2}, 0)$  and radius  $\frac{1}{2}$ . For  $\beta = 0.5$  and all values of  $k$  considered, the (50) smallest eigenvalues of  $A_\beta^{-1}A$  also inside the circle but more clustered around  $(0.05, 0)$ .

In our first experiment we solve the linear system preconditioned with matrix  $A_\beta$  for  $\beta = 0.1$  and  $\beta = 0.5$ . The results are reported in Table 2. Observe that as the value of  $k$  is increased, the order  $N$  of the linear system is bigger and the CPU time to reach GMRES convergence is increased. However, the relative residual in the last step of GMRES is of order  $10^{-7}$  in all cases.

In practice CSLP matrix (44) is approximated by  $\tilde{A}_\beta$  obtained from ILU factorization of  $A_\beta$  with drop tolerance  $\varepsilon$ . In the second row of Fig. 7 we show the (50) smallest in magnitude eigenvalues of  $\tilde{A}_\beta^{-1}A$ , for  $\tilde{A}_\beta$  computed with  $\beta = 0.1, \varepsilon = 10^{-2}$ . Comparing the first and the second row of Fig. 7, we observe that the eigenvalues of  $\tilde{A}_\beta^{-1}A$  are relatively good approximations of the eigenvalues of  $A_\beta^{-1}A$ , even when ILU factorization of  $A_\beta$  has a low computational cost, since it was computed with a relatively high drop tolerance  $\varepsilon = 10^{-2}$ . The approximation of the eigenvalues is even better if  $\tilde{A}_\beta$  is computed with  $\beta = 0.5$  and  $\varepsilon = 10^{-2}$ . But this is not always the case, for

**Table 2**  
Performance of GMRES preconditioned with CSLP  $A_\beta$ .

$k$ ( $m^{-1}$ )	$N$	Time GMRES (s)		# iter GMRES		Rel. residual	
		$\beta = 0.1$	$\beta = 0.5$	$\beta = 0.1$	$\beta = 0.5$	$\beta = 0.1$	$\beta = 0.5$
418.9	30 000	29.93	120.69	23	88	$7.40 \times 10^{-7}$	$7.03 \times 10^{-7}$
1 256.6	37 400	41.85	164.33	23	89	$6.73 \times 10^{-7}$	$7.16 \times 10^{-7}$
2 094.4	50 000	60.42	241.66	23	88	$7.06 \times 10^{-7}$	$7.10 \times 10^{-7}$

**Table 3**  
Performance of GMRES preconditioned with  $\tilde{A}_\beta$  obtained with ILU factorization of CSLP  $A_\beta$  with  $\beta = 0.1$  and two values of  $\varepsilon$ :  $\varepsilon_1 = 10^{-4}$  and  $\varepsilon_2 = 10^{-2}$ .

$k$ ( $m^{-1}$ )	$N$	Time ILU (s)		Time GMRES (s)		Total time (s)		# iter GMRES	
		$\varepsilon_1$	$\varepsilon_2$	$\varepsilon_1$	$\varepsilon_2$	$\varepsilon_1$	$\varepsilon_2$	$\varepsilon_1$	$\varepsilon_2$
418.9	30 000	10.47	1.69	3.87	2.85	14.34	<b>4.54</b>	24	81
1 256.6	37 400	15.19	4.98	5.19	7.81	20.38	<b>12.79</b>	24	89
2 094.4	50 000	21.76	3.05	6.85	11.64	28.61	<b>14.69</b>	24	211

**Table 4**  
Performance of GMRES preconditioned with  $\tilde{A}_\beta$  obtained with ILU factorization of CSLP  $A_\beta$  with  $\beta = 0.5$  and two values of  $\varepsilon$ :  $\varepsilon_1 = 10^{-4}$  and  $\varepsilon_2 = 10^{-2}$ .

$k$ ( $m^{-1}$ )	$N$	Time ILU (s)		Time GMRES (s)		Total time (s)		# iter GMRES	
		$\varepsilon_1$	$\varepsilon_2$	$\varepsilon_1$	$\varepsilon_2$	$\varepsilon_1$	$\varepsilon_2$	$\varepsilon_1$	$\varepsilon_2$
418.9	30 000	3.53	1.25	6.02	4.37	9.55	<b>5.62</b>	89	147
1 256.6	37 400	4.98	1.72	7.81	6.16	12.79	<b>7.88</b>	89	163
2 094.4	50 000	10.56	2.52	11.04	8.65	21.60	<b>11.17</b>	89	177

instance for  $\beta = 1/k$  and  $\varepsilon = 10^{-2}$  the eigenvalues of  $\tilde{A}_\beta^{-1}A$  are a very poor approximation of the eigenvalues of  $A_\beta^{-1}A$  and some of them are even outside of the circle.

In **Tables 3** and **4** we summarize the performance of GMRES, with the preconditioner  $\tilde{A}_\beta$  computed with  $\beta = 0.1$  and  $\beta = 0.5$  respectively. In both cases two values of drop tolerance for ILU factorization are considered:  $\varepsilon_1 = 10^{-4}$  and  $\varepsilon_2 = 10^{-2}$ . In columns 3 and 4 of both tables we report respectively the time (in seconds  $s$ ) for computing ILU factorization of  $A_\beta$  and the time for GMRES convergence. Since  $N$  is increased with  $k$ , both times are also increased with  $k$ . Column 5 contains the sum of the times for ILU factorization and GMRES convergence. Observe that the number of GMRES iterations reported in column 6 is increased with  $k$  for  $\varepsilon_2$  and remains constant for  $\varepsilon_1$ . The relative residual of the preconditioner system is of order  $10^{-7}$  for all values of  $k$ ,  $\beta$  and  $\varepsilon$  included in the study.

Comparing the times reported in **Table 2** (column 3 for  $\beta = 0.1$ ) and **Table 3** (columns 5 and for both  $\varepsilon_1$  and  $\varepsilon_2$ ) it is clear that preconditioner  $\tilde{A}_\beta$  is computationally more efficient than the exact CSLP preconditioner  $A_\beta$ , since GMRES takes advantage of the factors  $L$  and  $U$  obtained from ILU factorization, for the solution of a sequence of systems with matrix  $\tilde{A}_\beta$  (and different right hand side). Similar observation holds comparing times reported in **Table 2** (column 3 for  $\beta = 0.5$ ) and **Table 4** (column 5 for both  $\varepsilon_1$  and  $\varepsilon_2$ ). For each value of  $k$  we highlight in **Tables 3** and **4** the minimum total time required for solving the linear system. Note that for both:  $\beta = 0.1$  and  $\beta = 0.5$ , the matrix  $\tilde{A}_\beta$  computed with drop tolerance  $\varepsilon_2 = 10^{-2}$  is the best preconditioner in the sense that GMRES converges in the minimum time.

From our experiments we conclude that matrix  $\tilde{A}_\beta$  obtained from ILU factorization of CSLP matrix  $A_\beta$  with  $\beta = 0.5$  and drop tolerance  $\varepsilon = 10^{-2}$ , is a very good preconditioner if GMRES is used to solve the linear system (42) derived from IgA discretization of radiation problem.

#### 4.2.3. Selecting the dimension of IgA approximation space

The application of IgA approach requires the selection of the numbers  $n$  and  $m$  defining the dimension  $N_{IgA} = nm$  of the IgA spline approximation space. In this section we show, by means of several experiments, that the

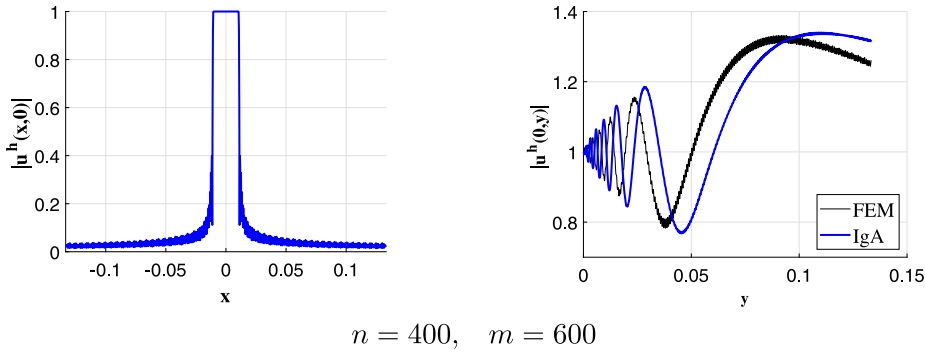


**Fig. 8.** IgA bicubic solution of radiation problem with  $f = 1.0$  MHz for  $n = 400$  and  $m = 600$ . Left: function  $|u^h(x, 0)|$ , right  $|u^h(0, y)|$ . Black: function  $|u_{FEM}(0, y)|$  computed with cubic FEM.

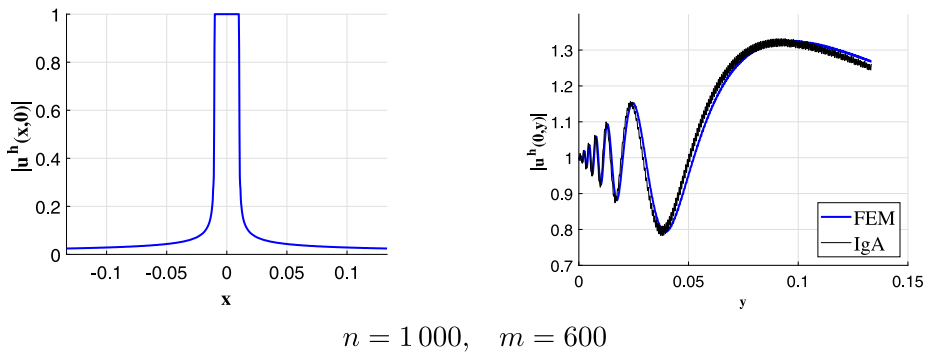


**Fig. 9.** IgA bicubic solution of radiation problem with  $f = 1.0$  MHz for  $n = 1000$  and  $m = 600$ . Left: function  $|u^h(x, 0)|$ , right  $|u^h(0, y)|$ . Black: function  $|u_{FEM}(0, y)|$  computed with cubic FEM.

numbers  $n$  and  $m$  play different roles in the accuracy of the IgA solution of the radiation problem. Moreover, we give some recommendations about the selection of  $n$  and  $m$  for the geometry of the domain considered in the paper.

From the physics of the radiation problem, it is known that most oscillations of acoustic pressure hold for  $-a \leq x \leq a$ . Hence, our analysis is based on the study of the behavior of the function  $|u^h(0, y)|$  for  $0 \leq y \leq r$ .

To illustrate the typical situation we solve the radiation problem for  $f = 1.0$  MHz, in the semicircle  $\Omega$  with  $r = 0.133$  m and  $a = 0.01$  m. Since  $n$  is the number of degrees of freedom in the direction  $x$ , perpendicular to wave front, if  $n$  is not large enough the function  $|u^h(x, 0)|$  is not a good approximation of  $|u(x, 0)|$ , in particular for  $x$  tending to one of the extremes of the transducer, with  $|x| > a$ . In Fig. 8 left, we observe this situation when radiation problem is solved with  $n = 400$  and  $m = 600$ . In this case the approximated solution behaves physically like the exact solution corresponding a width larger than  $2a$ . This is observed in Fig. 8 right, where we compare  $|u^h(0, y)|$  with the function  $|u_{FEM}(0, y)|$  computed with cubic Lagrange FEM and 3 338 722 degrees of freedom. FEM solution used as reference was obtained after a convergence study for several mesh sizes. Observe that function  $|u^h(0, y)|$  has a different phase and amplitude than the reference function  $|u_{FEM}(0, y)|$ . This behavior has been already observed in FEM [5], solving a 1D Helmholtz problem, for which exact solution is known. In Fig. 9 we show the effect of increasing the value of  $n$  from 400 to 1000 (preserving  $m = 600$ ). For increasing  $n$ , the corresponding solution  $|u^h(x, 0)|$  becomes a better approximation of  $|u(x, 0)|$  and the error in phase and amplitude between  $|u^h(0, y)|$  and  $|u_{FEM}(0, y)|$  is significantly reduced, see Fig. 9, right.

Concerning the number  $m$  of degrees of freedom in direction  $y$ , longitudinal to wave front, we have observed that it is tied up with the noise. More precisely, if  $m$  is not large enough, then the quality along  $y$  axis of the approximated solution is poor. Hence, the graph of the function  $|u^h(0, y)|$  is noisy, specially in far field region, which is the most interesting in ultrasonic applications. In Fig. 10 left we show the graph of  $|u^h(0, y)|$  obtained with IgA approach for  $n = 1000$  and  $m = 300$ . Observe that for this value of  $m$ ,  $|u^h(0, y)|$  suffers from a severe

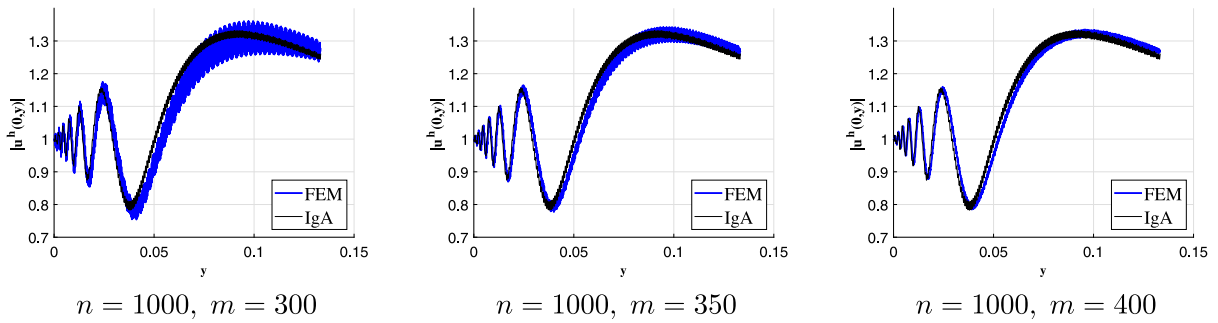


**Fig. 10.** Solution of the radiation problem with  $f = 1.0$  MHz. Black: function  $|u_{FEM}(0, y)|$  computed with cubic FEM. Blue: function  $|u^h(0, y)|$  computed with bicubic IgA for increasing  $m$ . (For interpretation of the references to color in this figure legend, the reader is referred to the web version of this article.)

noise. This problem is solved gradually if we increase the value of  $m$  first to  $m = 350$  (Fig. 10 center) and later to  $m = 400$  (Fig. 10 right).

To guarantee the accuracy of the numerical solution both FEM and IgA require that mesh size be fine enough. In practice the rule of thumb  $h_{IgA} = \lambda/\tau = 2\pi/(\tau k)$  is frequently used, where  $\tau \geq 10$  denotes the number of degrees of freedom per wavelength. Nevertheless, for high values of  $k$  this is not enough, since for  $h_{IgA}$  satisfying the rule of thumb, the pollution error is reduced significantly but it does not disappear [23,26].

By definition the mesh size  $h_{IgA}$  is the maximum length of an edge of the mesh  $\mathcal{K}$ , with vertices  $\mathbf{F}_\theta(\xi_i, \eta_j)$  for  $i = 1, \dots, n - 2$  and  $j = 1, \dots, m - 2$ . Thus, the value of  $h_{IgA}$  not only depends on  $n$  and  $m$ , but also on the parametrization  $\mathbf{F}_\theta(\xi, \eta)$  of  $\Omega$ . This dependency is nonlinear and in consequence it is not feasible to find explicit expressions for  $n$  and  $m$  in terms of the input parameters  $r, \tau$  and  $k$  in order to achieve  $h_{IgA} = \lambda/\tau$ . Nevertheless, it is possible to obtain lower bounds for  $n$  and  $m$  that are useful in practice. Let be  $h_x = 2r/(n-3)$  and  $h_y = r/(m-3)$ . Since  $\mathbf{F}_\theta(\xi, \eta)$  maps linearly  $(\xi, 0), 0 \leq \xi \leq 1$  in  $(x, 0)$  with  $-r \leq x \leq r$ , it is clear that  $h_{IgA} \geq h_x$ . Moreover, taking into account that  $\Omega$  is symmetric with respect to  $y$ -axis and that  $\mathbf{F}_\theta(\xi, \eta)$  satisfies the symmetry condition  $\mathbf{F}_\theta(\frac{1}{2} - \varepsilon, \eta) = \mathbf{F}_\theta(\frac{1}{2} + \varepsilon, \eta)$ , it holds that  $h_{IgA} \geq h_y$ . Hence  $h_{IgA} > 2r/n$  and  $h_{IgA} > r/m$ . From the rule of thumb  $h_{IgA} = \lambda/\tau$  we obtain the following lower bounds for  $n$  and  $m$ ,

$$n > \frac{2r\tau}{\lambda}, \quad m > \frac{r\tau}{\lambda} \tag{47}$$

For  $n$  and  $m$  big enough the lower bounds in (47) are very close to  $n$  and  $m$ , in consequence it is recommended to choose  $n \geq 2m$ . On the other hand, to select  $n = \mu m$  with  $\mu \gg 2$  is not a good strategy since in comparison with the case  $n = 2m$ , the number of degrees of freedom is larger, thus the computational cost is bigger, while the mesh size remains equal.

### 4.3. Comparing IgA with FEM

In this section we evaluate the performance of isogeometric approach comparing the IgA approximation with the solution of the radiation problem obtained using classic FEM. In order to do a fair comparison we perform first a convergence study to select the IgA approximated solution that will be used as reference for comparison with FEM.

In the rest of the section, IgA approximated solution  $u^h$  is sought in a bicubic tensor product spline space  $\mathbb{S}_{4,t^\xi} \otimes \mathbb{S}_{4,t^\eta}$ , where the sequence  $t^\eta$  with  $m + 4$  knots has uniform breakpoints. The sequence of knots  $t^\xi$  is constructed inserting the points  $\xi_{a^-}$  and  $\xi_{a^+}$  defined by (25) as simple knots in the sequence  $\widehat{t}^\xi$  with  $\mu m + 4$  knots and uniform breakpoints. Observe that the total number  $n$  of elements of  $t^\xi$  is now  $n + 4$  with  $n = \mu m + z$ , where  $z$  is equal to 0,1 or 2 depending on whether the points  $\xi_{a^-}$  and  $\xi_{a^+}$  were already contained in  $\widehat{t}^\xi$ . Imposing that  $\xi_{a^-}$  and  $\xi_{a^+}$  belong to  $t^\xi$  the solution space is enriched at  $x = \pm a$  and the eventual spillover restrictions on basis functions outside  $(-a, a)$  due to Dirichlet boundary condition is mitigated. Consequently, Neumann condition is better approximated resulting in a more accurate numerical solution  $u^h$ .

**Table 5**

Data for convergence study for  $k = 3141.6 \text{ m}^{-1}$ .

$n$	392	412	432	452	472	492	512	532	552	<b>612</b>
$m$	195	205	215	225	235	245	255	265	275	<b>305</b>
$\tau$	3.68	3.87	4.06	4.25	4.44	4.63	4.83	5.02	5.21	<b>5.79</b>

**Table 6**

Data for convergence study for  $k = 4188.8 \text{ m}^{-1}$ .

$n$	702	732	782	812	862	892	942	972	1022	<b>1102</b>
$m$	350	365	390	405	430	445	470	485	510	<b>550</b>
$\tau$	3.74	3.90	4.17	4.33	4.60	4.76	5.03	5.19	5.46	<b>5.89</b>

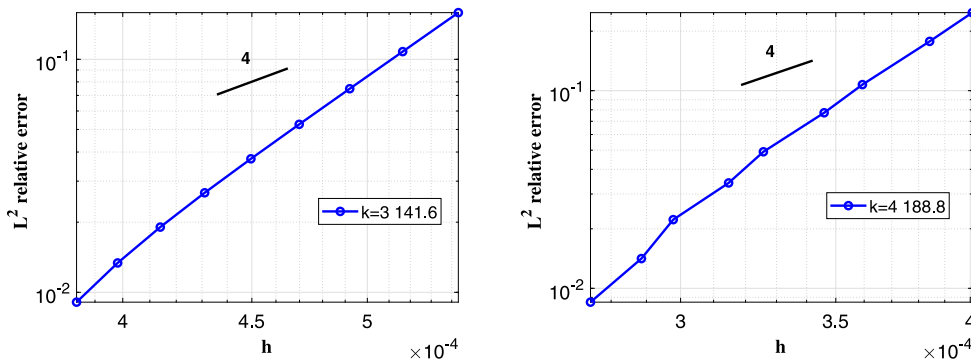


**Fig. 11.** Relative errors (48) for IgA bicubic solutions of the radiation problem for  $k = 3141.6 \text{ m}^{-1}$  (left) and  $k = 4188.8 \text{ m}^{-1}$  (right).

4.3.1. Convergence study

Our aim in this section is to perform a brief convergence study based on  $h$  refinement for computing IgA solution of the radiation problem. For each value  $m$  of an increasing sequence, we compute the uniform sequence  $t^n$  and the knot sequence  $t^\xi$  as explained before with  $\mu = 2$ . The approximated solution  $u^h$  with  $nm$  degrees of freedom is computed with IgA bicubic B-spline functions using the parametrization  $\mathbf{F}_\theta$  introduced in 3.2 with  $\theta = \pi/4$ . We solve two radiation problems in a semicircular domain  $\Omega$  with width  $a = 0.01 \text{ m}$ . In the first problem  $k = 3141.6 \text{ m}^{-1}$ , and  $r = 0.100 \text{ m}$ . In the second problem  $k = 4188.8 \text{ m}^{-1}$ , and  $r = 0.133 \text{ m}$ . In Tables 5 and 6 we summarize the input values of  $n$  and  $m$  for each problem. The corresponding mesh size  $h$  is written as  $h = \lambda/\tau$ . In the third row of both tables it is included the number  $\tau$  of degrees of freedom per wavelength. We use as reference solution  $u_{ref}^h$ , the IgA approximation computed with the parameters reported in bold in the last column of Tables 5 and 6. Moreover, we compute the relative errors,

$$relerr = \frac{\|u_{ref}^h - u^h\|_{L^2(\Omega)}}{\|u_{ref}^h\|_{L^2(\Omega)}} \tag{48}$$

In Fig. 11 we show the log–log plot of the relative error versus the mesh size  $h$ . For reference, we also show in the graph the line with slope 4. It is clear that the rate of convergence of the relative error is  $h^4$ , as theory predicts [10] for a bicubic IgA approximation. In the next section we use these reference solutions (and the reference solution computed similarly for  $k = 5235.9$ ) for comparison with FEM solution.

4.3.2. Comparison

Unfortunately, it is difficult to compare with FEM approximations of similar problems obtained by other authors, since most of them do not report all the information needed to set up a fair comparison, such as the type of elements and the number of degrees of freedom. Hence, in this section we solve the radiation problem with FEM and IgA approaches, using in both cases piecewise cubic polynomials. FEM approximation was computed with COMSOL [2] using a PC with an i5 processor of 10th generation and 32 Gb of RAM.

**Table 7**  
Parameters for IgA solution of the radiation problem for comparison with FEM.

$f$ (MHz)	$k$ ( $m^{-1}$ )	$r$ (m)	$n$	$m$	$h_{IgA}$ (m)
0.75	3 141.6	0.100	612	305	$3.45 \times 10^{-4} = \lambda/5.79$
1.00	4 188.8	0.133	1102	550	$2.54 \times 10^{-4} = \lambda/5.89$
1.25	5 235.9	0.166	1802	800	$2.18 \times 10^{-4} = \lambda/5.50$

In the next experiments we consider three values of frequency:  $f = 0.75$  MHz,  $f = 1.0$  MHz and  $f = 1.25$  MHz. The semi-width  $a$  is always fixed as 0.01 m, but the radius  $r$  of the semicircle depends on the frequency and it is computed as  $r = 2N_f = \frac{a^2 k}{\pi}$ . Since the wavelength  $\lambda$  and the frequency  $f$  are inversely proportional, if  $f$  is of order 1 MHz, then  $\lambda$  is of order  $10^{-3}$  m, which means that the solution  $u(x, y)$  is highly oscillatory. As we already mentioned, for such values of frequency, classic FEM solves the Helmholtz equation using a mesh of size  $h_{FEM}$ , with  $h_{FEM} \leq \frac{\lambda}{10}$ . As a consequence, the approximated solutions depend on a high number of degrees of freedom. FEM approximation is computed with cubic Lagrange polynomials defined on a quadrilateral mesh. The problem was solved with FEM several times using different values of  $h_{FEM}$ , with  $\frac{\lambda}{5} \leq h_{FEM} \leq \frac{\lambda}{10}$ . Since the results obtained were very similar, we select the solution with less degrees of freedom (corresponding to  $h_{FEM} = \frac{\lambda}{5}$ ) as the reference for the comparison with IgA. For computing IgA solution we use the bicubic B-splines with the knots sequences  $t^\xi$  and  $t^\eta$  constructed as explained at the beginning of Section 4.3. Moreover, the domain  $\Omega$  is parametrized by means of the map  $\mathbf{F}_\theta(\xi, \eta)$  described in Section 3.2 for  $\theta = \pi/4$ .

In Table 7 we summarize, for each frequency  $f$ , the values in the experiments of the wavenumber  $k$ , the radius  $r$  and the numbers  $n, m$  defining the dimension  $N_{IgA} = nm$  of the bicubic B-spline approximation space. Moreover, in the last column of the table we report the size  $h_{IgA}$  of the mesh  $\mathcal{K}$  defined in Section 3.3.2. In our experiments we have observed that for obtaining a precise approximated solution  $u^h(x, y)$  of the radiation problem, it is enough to select the dimension  $N_{IgA}$  of the approximation space (22) in such a way that  $h_{IgA} \approx \frac{\lambda}{6}$ .

Since the maximum amplitude of the acoustic wave pressure is attained on the profile  $x = 0$ , our comparison focus on the behavior of the function  $|u^h(0, y)|$ . In Fig. 12 we show the graph of the functions  $|u^h(0, y)|$  obtained using FEM (first row) and IgA (second row) approaches. From the physical point of view, we observe that both provide solutions with similar behavior: for increasing frequency the number of oscillations of  $|u^h(0, y)|$  in the near field region grows, but in any case from the natural focus on there are no more oscillations and the maximum amplitude of the acoustic wave is reached.

Nevertheless, comparing the functions  $|u^h(0, y)|$  computed with FEM and IgA it is clear that, for all values of frequencies, FEM approximation has more noise, even when the number  $N_{FEM}$  of degrees of freedom used for its computation is several times bigger (5.66, 5.51 and 5.65 for frequencies  $f = 0.75$  MHz,  $f = 1.0$  MHz and  $f = 1.25$  MHz respectively), than the number  $N_{IgA}$  of degrees of freedom used for the computation with IgA approach. In Fig. 13 we show a zoom of the rectangular area in right column of Fig. 12. Observe that the noise of the function  $|u^h(0, y)|$  computed with FEM has higher frequency and larger amplitude than the noise of the function  $|u^h(0, y)|$  computed with IgA for the same  $f = 1.25$  MHz.

### 5. Conclusions

Radiation problem appears in several important applications, where high values of the wavenumber are handled. We have solved this problem in a 2D scenario, with one transducer emitting a pulse of constant amplitude and high frequency. The unknown of the radiation problem is the acoustic pressure field, that from the mathematical point of view is the solution of Helmholtz equation with mixed boundary conditions.

For high values of the wavenumber, the classical method of Finite Element suffers from the pollution error and requires a large number of degrees of freedom to obtain accurate solutions. Isogeometric Analysis was proposed as an advantageous alternative to FEM. Fundamental steps of the method were discussed with focus on several details that are not usually described in the literature. In particular, we proposed a quadratic NURBS parametrization of the physical domain  $\Omega$ , that represents exactly its boundary and depends on a free parameter. The approximated solution  $u^h$  was computed using a non-isoparametric approach, where  $u^h$  is a bicubic tensor product polynomial B-spline function on  $\Omega$ . This approach turned out to be very useful in practice, since it allows to improve the accuracy of  $u^h$  refining the approximation space and keeping the coarser parametrization of  $\Omega$ . For the problem under consideration

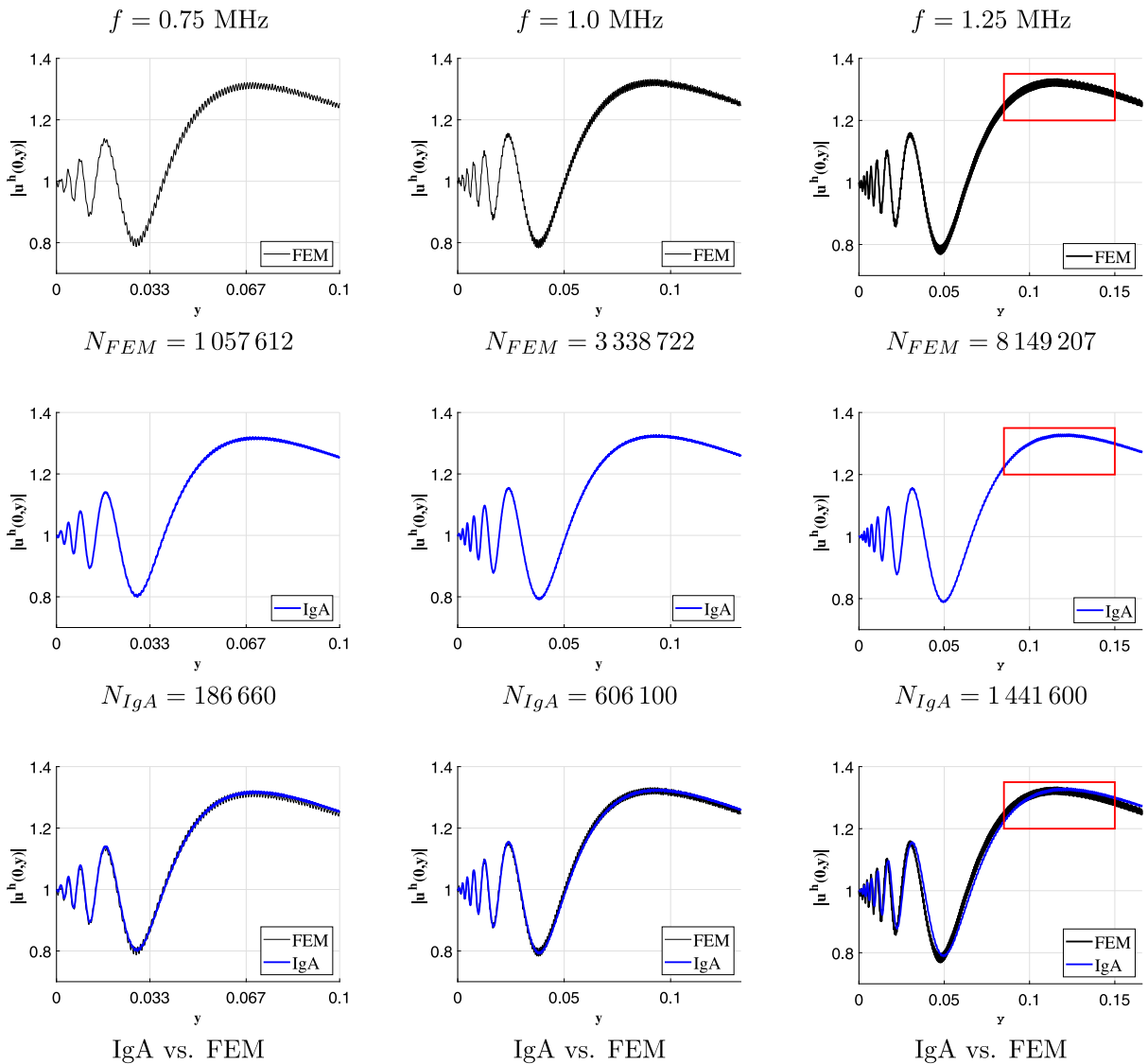


**Fig. 12.** Graphs of the function  $|u^h(0, y)|$  for several values of the frequency  $f$ . Top:  $u^h(x, y)$  computed with cubic Lagrange FEM with a quadrilateral mesh. Center:  $u^h(x, y)$  computed with cubic B-splines. The total number of degrees of freedom is given for each case. Bottom: comparison between FEM and IgA solutions for the same frequency. Left column:  $f = 0.75$  MHz, center column:  $f = 1.0$  MHz, right column:  $f = 1.25$  MHz.

we obtained a deeper understanding of the role of the number of degrees of freedom in each parametric direction. Through several experiments we have shown that increasing the degrees of freedom in the direction longitudinal to wave front reduces the noise of  $u^h$ , while increasing the degrees of freedom in the perpendicular direction reduces the phase and amplitude shifts of  $u^h$ . Moreover, the experiments also bring evidences of the impact of the parametrization on the accuracy of  $u^h$ . For both, FEM and IgA approaches, the discretization process leads to large, complex and ill-conditioned linear systems, as  $k$  grows. We studied the performance of GMRES to solve the linear system derived from IgA discretization of the radiation problem. Our studies have confirmed that in IgA context, Complex Shifted Laplacian is also a very good preconditioner for the linear system derived from the discretization of Helmholtz equation with mixed boundary conditions.

We have implemented IgA approach using the open source package GeoPDEs. The experiences obtained from the intensive experimentation with our code confirm that compared to FEM, IgA produces smoother solutions with

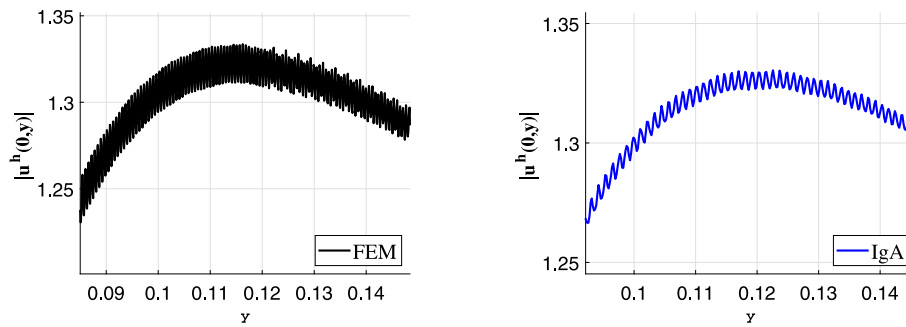


**Fig. 13.** Zoom of rectangular area shown in right column of Fig. 12 ( $f = 1.25$  MHz). Left: function  $|u^h(0, y)|$  computed with FEM, right: function  $|u^h(0, y)|$  computed with IgA.

smaller pollution errors and substantially less degrees of freedom. Thanks to the skills and experiences acquired in the solution of the 2D homogeneous radiation problem, we will be able in the near future to tackle more realistic radiation problems, where an array of transducers emits the pulse in an heterogeneous medium.

### Acknowledgments

Authors V. Hernández Mederos, E. Moreno Hernández and J. Estrada Sarlabous were partially supported by the National Research Program: Automática, Robótica e Inteligencia Artificial, Cuba. The authors thank the anonymous referees for their very useful comments and suggestions.

### References

- [1] I.A. Abelló Ugalde, V. Hernández Mederos, P. Barrera Sánchez, G. González Flores, Injectivity of B-spline biquadratic maps, *Comput. Methods Appl. Mech. Engrg.* 341 (2018) 586–608.
- [2] Anon, COMSOL Multiphysics, Version 5.5, COMSOL Company, Sweden.
- [3] X. Antoine, T. Khajah, NURBS-based isogeometric analysis of standard and phase reduction on-surface radiation condition formulations for acoustic scattering, *Comput. Methods Appl. Mech. Engrg.* 392 (2022) 114700.
- [4] E. Atroshchenko, A. Calderon Hurtado, C. Anitescu, T. Khajah, Isogeometric collocation for acoustic problems with higher-order boundary conditions, *Wave Motion* 110 (9) (2020) 102861.
- [5] I. Babuška, F. Ihlenburg, T. Strouboulis, S.K. Gangaraj, A posteriori error estimation for finite element solutions of Helmholtz equation, part i, *Internat. J. Numer. Methods Engrg.* 40 (1997) 3443–3462.
- [6] I. Babuška, S.A. Sauter, Is the pollution effect of the FEM avoidable for the Helmholtz equation considering high wave number?, *SIAM J. Numer. Anal.* 34 (1997) 2392–2423; Reprinted in, *SIAM Review* 42 (2000) 451–484;
- [7] A. Bayliss, M. Gunzburger, E. Turkel, Boundary conditions for the numerical solution of elliptic equations in exterior regions *SIAM J. Appl. Math.* 42 (2) (1982) 430–451.
- [8] A. Bayliss, E. Turkel, Far field boundary conditions for compressible flows *J. Comput. Phys.* 48 (1982) 182–199.
- [9] I. Bazán, M. Vázquez, A. Ramos, A. Vera, L. Leija, A performance analysis of echographic ultrasonic techniques for non-invasive temperature estimation in hyperthermia range using phantoms with scatterers *Ultrasonics* 49 (2009) 358–376.
- [10] Y. Bazilevs, L. Beirão Da Veiga, J. Cottrell, T.J.R. Hughes, G. Sangalli, Isogeometric analysis: Approximation, stability and error estimates for h-refined meshes *Math. Models Methods Appl. Sci.* 16 (7) (2006) 1031–1090.
- [11] M. Brovka, Construction of Polynomial Spline Spaces over T-Meshes for Its Application in Isogeometric Analysis (Ph.D. thesis), Universidad de Las Palmas de Gran Canaria, 2016.
- [12] A. Buffa, G. Sangalli, R. Vázquez, Isogeometric analysis in electromagnetics: B-splines approximation *Comput. Methods Appl. Mech. Engrg.* 199 (17) (2010) 1143–1152.
- [13] L. Chen, H. Lian, Z. Liu, H. Chen, E. Atroshchenko, S.P.A. Bordas, Structural shape optimization of three dimensional acoustic problems with isogeometric boundary element methods *Comput. Methods Appl. Mech. Engrg.* 355 (2019) 926–951.
- [14] L. Chen, H. Lian, S. Natarajan, W. Zhao, X. Chen, S.P.A. Bordas, Multi-frequency acoustic topology optimization of sound-absorption materials with isogeometric boundary element methods accelerated by frequency-decoupling and model order reduction techniques *Comput. Methods Appl. Mech. Engrg.* 395 (2022) 114997.
- [15] L. Chen, C. Liu, W. Zhao, L. Liu, An isogeometric approach of two dimensional acoustic design sensitivity analysis and topology optimization analysis for absorbing material distribution *Comput. Methods Appl. Mech. Engrg.* 336 (2018) 507–532.
- [16] L. Chen, C. Lu, H. Lian, Z. Liu, W. Zhao, S. Li, H. Chen, S.P.A. Bordas, Acoustic topology optimization of sound absorbing materials directly from subdivision surfaces with isogeometric boundary element methods *Comput. Methods Appl. Mech. Engrg.* 362 (2020) 112806.

- [17] L. Coox, O. Atak, D. Vandepitte, W. Desmet, An isogeometric indirect boundary element method for solving acoustic problems in open-boundary domains *Comput. Methods Appl. Mech. Engrg.* 316 (2017) 186–208.
- [18] L. Coox, E. Deckers, D. Vandepitte, W. Desmet, A performance study of NURBS-based isogeometric analysis for interior two dimensional time-harmonic acoustics *Comput. Methods Appl. Mech. Engrg.* 305 (2016) 441–467.
- [19] J.A. Cottrell, T.J.R. Hughes, Y. Bazilevs, *Isogeometric Analysis: Toward Integration of CAD and FEA*, John Wiley, 2009.
- [20] M. Cruz, V. Hernández, J. Estrada, E. Moreno, A. Mansur, Numerical solution of the wave propagation problem in a plate *J. Theor. Comput. Acoust.* 30 (2) (2022) 2150014.
- [21] C. de Falco, A. Reali, R. Vázquez, Geopdes: a research tool for isogeometric analysis of PDEs *Adv. Eng. Softw.* 42 (12) (2011) 1020–1034.
- [22] M. Dinachandra, R. Sethuraman, Plane wave enriched partition of unity isogeometric analysis (PUIGA) for 2D Helmholtz problems *Comput. Methods Appl. Mech. Engrg.* 335 (2018) 380–402.
- [23] G.C. Diwan, M.S. Mohamed, Pollution studies for high order isogeometric analysis and finite element for acoustic problems *Comput. Methods Appl. Mech. Engrg.* 350 (2019) 701–718.
- [24] G.C. Diwan, M.S. Mohamed, Iterative solution of Helmholtz problem with high-order isogeometric analysis and finite element method at mid-range frequencies *Comput. Methods Appl. Mech. Engrg.* 363 (2020) 112855.
- [25] S.M. Dsouza, T. Khajah, X. Antoine, S.P.A. Bordas, S. Natarajan, Non uniform rational B-splines and Lagrange approximations for time-harmonic acoustic scattering: accuracy and absorbing boundary conditions *Math. Comput. Model. Dyn. Syst.* 27 (1) (2021) 290–321.
- [26] V. Dwarka, R. Tielen, M. Möller, C. Vuik, Towards accuracy and scalability: Combining isogeometric analysis with deflation to obtain scalable convergence for the Helmholtz equation *Comput. Methods Appl. Mech. Engrg.* 377 (2021) 113694.
- [27] Y.A. Erlangga, C. Vuik, C.W. Oosterlee, On a class of preconditioners for solving the Helmholtz equation *Appl. Numer. Math.* 50 (3–4) (2004) 409–425.
- [28] O.G. Ernst, M.J. Gander, Why it is difficult to solve Helmholtz problems with classical iterative methods? in: *Numerical Analysis of Multiscale Problems*, 2011, pp. 325–363.
- [29] H. Espinoza, R. Codina, S. Badia, A sommerfeld non-reflecting boundary condition for the wave equation in mixed form *Comput. Methods Appl. Mech. Engrg.* 276 (2014) 122–148.
- [30] K. Gahalaut, S. Tomar, Condition Number Estimates for Matrices Arising in the Isogeometric Discretizations, RICAM Report, 23, 2012.
- [31] M.J. Gander, I.G. Graham, E.A. Spence, Applying GMRES to the Helmholtz equation with shifted Laplacian preconditioning: what is the largest shift for which wavenumber-independent convergence is guaranteed? *Numer. Math.* 131 (3) (2015) 567–614.
- [32] M.I. Gutiérrez, H. Calás, A. Ramos, A. Vera, L. Leija, Acoustic field modeling for physiotherapy ultrasound applicators by using approximated functions of measured non-uniform radiation distributions *Ultrasonics* 52 (2012) 767–777.
- [33] V. Hernández, J. Estrada, E. Moreno, S. Rodríguez, A. Mansur, Numerical solution of a wave propagation problem along plate structures based on the isogeometric approach *J. Comput. Acoust.* 26 (1) (2018) 1750030.
- [34] T.J.R. Hughes, J.A. Cottrell, Y. Bazilevs, Isogeometric analysis: CAD, finite elements, NURBS, exact geometry and mesh refinement *Comput. Methods Appl. Mech. Engrg.* 194 (39–41) (2005) 4135–4195.
- [35] F. Ihlenburg, I. Babuška, Finite element solution of Helmholtz equation with high wave number. Part I: the h-version of FEM *Comput. Math. Appl.* 30 (9) (1995) 9–37.
- [36] Z. Izadifar, Z. Izadifar, D. Chapman, P. Babyn, An introduction to high intensity focused ultrasound: Systematic review on principles, devices, and clinical applications *J. Clin. Med.* 9 (2020) 460.
- [37] T. Khajah, X. Antoine, S.P.A. Bordas, Isogeometric finite element analysis of time-harmonic exterior acoustic scattering problems 2016, arXiv preprint 1610.01694.
- [38] T. Khajah, V. Villamizar, Highly accurate acoustic scattering: Isogeometric analysis coupled with local high order farfield expansion ABC *Comput. Methods Appl. Mech. Engrg.* 349 (2019) 477–498.
- [39] P.M. Knupp, Algebraic mesh quality metrics *SIAM J. Sci. Comput.* 23 (1) (2001) 193–218.
- [40] S. Lipton, J.A. Evans, Y. Bazilevs, T. Elguedj, T.J.R. Hughes, Robustness of isogeometric structural discretizations under severe mesh distortion *Comput. Methods Appl. Mech. Engrg.* 199 (2010) 357–373.
- [41] J.M. Melenk, I. Babuška, The partition of unity finite element method: Basic theory and applications *Comput. Methods Appl. Mech. Engrg.* 139 (1996) 289–314.
- [42] J. Melenk, S. Sauter, Convergence analysis for finite element discretizations of the Helmholtz equation with Dirichlet-to-Neumann boundary conditions *Math. Comp.* 79 (272) (2010) 1871–1914.
- [43] M.S. Mohamed, A. El-Kacimi, O. Laghrouche, Some numerical aspects of the PUFEM for efficient solution of 2D Helmholtz problems *Comput. Struct.* 88 (2010) 1484–1491.
- [44] M.J. Peake, *Enriched and Isogeometric Boundary Element Methods for Acoustic Wave Scattering* (Durham theses), Durham University, 2014, Available at Durham E-Theses Online: <http://etheses.dur.ac.uk/10655/>.
- [45] M. Peake, J. Trevelyan, G. Coates, Extended isogeometric boundary element method (XIBEM) for two-dimensional Helmholtz problems *Comput. Methods Appl. Mech. Engrg.* 259 (2013) 93–102.
- [46] M.J. Peake, J. Trevelyan, G. Coates, Extended isogeometric boundary element method (XIBEM) for three-dimensional medium-wave acoustic scattering problems *Comput. Methods Appl. Mech. Engrg.* 284 (2015) 762–780.
- [47] H.H. Pennes, Analysis of tissue and arterial blood temperatures in the resting human forearm *J. Appl. Physiol.* 1 (2) (1948) 93–122.
- [48] L. Piegl, *The NURBS Book*, Springer, 1997.
- [49] A.M. Shaaban, *Isogeometric Boundary Element Analysis and Structural Shape Optimization for Helmholtz Acoustic Problems* (Ph.D. thesis), Bauhaus-Universität Weimar, 2022, <http://dx.doi.org/10.25643/bauhaus-universitaet.4703>.

- [50] A.M. Shaaban, C. Anitescu, E. Atroshchenko, T. Rabczuk, Isogeometric boundary element analysis and shape optimization by PSO for 3D axi-symmetric high frequency Helmholtz acoustic problems *J. Sound Vib.* 486 (2020) 115598.
- [51] A.M. Shaaban, C. Anitescu, E. Atroshchenko, T. Rabczuk, Shape optimization by conventional and extended isogeometric boundary element method with PSO for two-dimensional Helmholtz acoustic problems *Eng. Anal. Bound. Elem.* 113 (2020) 156–169.
- [52] A.M. Shaaban, C. Anitescu, E. Atroshchenko, T. Rabczuk, 3D isogeometric boundary element analysis and structural shape optimization for Helmholtz acoustic scattering problems *Comput. Methods Appl. Mech. Engrg.* 384 (2021) 113950.
- [53] A. Shamanskiy, M. Gfrerer, J. Hinz, B. Simeon, Isogeometric parametrization inspired by large elastic deformation *Comput. Methods Appl. Mech. Engrg.* 363 (2020) 112920.
- [54] A.H. Sheikh, D. Lahaye, L. Garcia Ramos, R. Nabben, C. Vuik, Accelerating the shifted Laplace preconditioner for the Helmholtz equation by multilevel deflation *J. Comput. Phys.* 322 (2016) 473–490.
- [55] A.H. Sheikh, D. Lahaye, C. Vuik, On the convergence of shifted Laplace preconditioner combined with multilevel deflation *Numer. Linear Algebra Appl.* 20 (4) (2013) 645–662.
- [56] R. Simpson, S.P.A. Bordas, J. Trevelyan, T. Rabczuk, A two-dimensional isogeometric boundary element method for elastostatic analysis *Comput. Methods Appl. Mech. Engrg.* 209–212 (2012) 87–100.
- [57] R. Simpson, M. Scott, M. Taus, D. Thomas, H. Lian, Acoustic isogeometric boundary element analysis *Comput. Methods Appl. Mech. Engrg.* 269 (2014) 265–290.
- [58] R. Martínez Valdez, A. Ramos Fernández, A. Vera Hernández, L. Leija Salas, Design of a low power hybrid HIFU applicator for haemostasis based on acoustic propagation modelling *Int. J. Hyperth.* (2015) <http://dx.doi.org/10.3109/02656736.2015.1112437>.
- [59] M.B. van Gijzen, Y.A. Erlanga, C. Vuik, Spectral analysis of the discrete Helmholtz operator preconditioned with a shifted Laplacian *SIAM J. Sci. Comput.* 29 (5) (2007) 1942–1958.
- [60] J.V. Venas, T. Kvamsdal, Isogeometric boundary element method for acoustic scattering by a submarine *Comput. Methods Appl. Mech. Engrg.* 359 (2020) 112670.
- [61] J.V. Venas, T. Kvamsdal, Isogeometric analysis of acoustic scattering with perfectly matched layers (IGAPML) *Comput. Methods Appl. Mech. Engrg.* 401 (2022) 115647.
- [62] J. Videla, C. Anitescu, T. Khajah, S. Bordas, E. Atroshchenko, h- and p-adaptivity driven by recovery and residual-based error estimators for PHT-splines applied to time-harmonic acoustics *Comput. Math. Appl.* 77 (9) (2019) 2369–2395.
- [63] W.A. Wall, M.A. Frenzel, C. Cyron, Isogeometric structural shape optimization *Comput. Methods Appl. Mech. Engrg.* 197 (2008) 2976–2988, 33–40.
- [64] Y.H. Wu, C.Y. Dong, H.S. Yang, Isogeometric indirect boundary element method for solving the 3D acoustic problems *J. Comput. Appl. Math.* 363 (2020) 273–299.
- [65] G. Xu, M. Li, B. Mourrain, T. Rabczuk, J. Xu, S.P.A. Bordas, Constructing IGA-suitable planar parameterization from complex CAD boundary by domain partition and global/local optimization *Comput. Methods Appl. Mech. Engrg.* 328 (2018) 175–200.
- [66] G. Xu, B. Mourrain, R. Duvigneau, A. Galligo, Constructing analysis-suitable parameterization of computational domain from CAD boundary by variational harmonic method *J. Comput. Phys.* 252 (2013) 275–289.
- [67] G. Xu, B. Mourrain, R. Duvigneau, A. Galligo, Optimal analysis-aware parameterization of computational domain in 3D isogeometric analysis *Comput. Aided Des.* 45 (2013) 812–821.
- [68] G. Xu, B. Mourrain, A. Galligo, T. Rabczuk, High-quality construction of analysis suitable trivariate NURBS solids by reparameterization methods *Comput. Mech.* 54 (5) (2014) 1303–1313.
- [69] Y. Zhang, Y. Bazilevs, S. Goswami, C.L. Bajaj, T.J.R. Hughes, Patient-specific vascular NURBS modeling for isogeometric analysis of blood flow *Comput. Methods Appl. Mech. Engrg.* 196 (29) (2007) 2943–2959.